INSTIITUTE OF ACCELERATING SYSTEMS AND APPLICATIONS, ATHENS, GREECE
WP10 Coordinator

MEDITERRANEAN OCEAN FORECASTING SYSTEM: TOWARD ENVIRONMENTAL PREDICTION

MFSTEP

Project Deliverable Report
D11

WP10: Atmospheric Forcing and Air-Sea Interaction Studies

Project title	**MEDITERRANEAN OCEAN FORECASTING SYSTEM: TOWARD ENVIRONMENTAL PREDICTION**
Project acronym	**MFSTEP**
Contract number	**EVK3-CT-2002-00075**
Deliverable number	**D11**
Deliverable title	**Studies of atmospheric response with sea-surface submodels**
Work package	**WP10 Atmospheric Forcing and Air-Sea Interaction Studies**
Name of WP10 Coordinator	**Prof. George Kallos** **Institute of Accelerating Systems and Applications, Athens, Greece**
Date of delivery	**February 28, 2005**
Report status	**Draft** **Final** **X**
Project home page	**http://www.bo.ingv.it/mfstep/**
WP10 home page	**http://forecast.uoa.gr/mfstep/**

1. Introduction

This report describes the work performed by IASA and ICoD under the scopes of deliverable 11 (subtask 10310) of WP10. This work package contains the necessary activities to create and deliver the atmospheric surface fields to the WP8 and WP9 ocean modelling community, to perform the Scientific Validation Period (SVP) intercomparison of atmospheric models, to study the sensitivity of the atmosphere to sea-surface conditions and to study the sensitivity of air-sea interaction to physical parameterizations. The aim of this sub-task (deliverable 11) is to improve and evaluate the model algorithms describing the air-sea interaction. More specifically, subtask 10310 relates to studying effects of the viscous sublayer model on atmospheric circulation conditions near the air-sea boundary. The viscous sublayer is a model component introduced in mid-90s in order to improve calculation of surface fluxes over the ocean.

The two groups made a series of experiments to fulfill the requirements of subtask 10310. Modeling experiments were performed over the MFSTEP-SVP period (January 2003) and the results shown in this report indicate the atmospheric response to the surface layer parameterization.

2. Numerical Models

IASA utilized the nonhydrostatic SKIRON/Eta modeling system which has been implemented in a large number of projects related to atmospheric and ocean forecasts, such as ANEMOS, AUTOHAZARD, ENVIWAVE, MAMCS, ADIOS and others. Recently, the IASA/AM&WFG group was involved in the preparation of weather, wave and air-quality forecasts for Athens Olympics. IASA/AM&WFG provided to the Hellenic National Meteorological Service very high-resolution forecasts as well as the SKIRON/Eta forecasts regularly provided at the framework of MFSTEP and ENVIWAVE projects.

Two atmospheric models have been used by ICoD: a) a standard version of the NCEP/Eta model implemented by ICOD in several other ocean-related EU projects (RAMSES, GAIANET, ADIOS, CLEOPATRA), and b) the most recent version of the non-hydrostatic NCEP/NMM model. Both models use the same parameterization scheme for representation of the viscous sublayer over the ocean (Janjic, 1994). The viscous sublayer has been introduced as additional model component as a response of the noticed errors in the atmospheric fluxes at the air-sea interface. The viscous sublayer regulates calculation of surface momentum, moisture and heat fluxes depending on the following mixing regimes: a) the Brownian mixing dominates over turbulent one; b) the Brownian and turbulent mixing are balanced; and when turbulent mixing dominates by seizing the viscous sublayer and generating a rough sea.

2.1 SKIRON/Eta modeling system

The SKIRON/Eta modeling system has been developed for operational use at the AM&WFG/IASA. The implementation of the system requires Unix computational environment and corresponding meteorological data input. The current version of the Eta model is appropriately coded in order to run on any parallel computer platform utilizing any number of processors (Kallos et al. 1997). The system has been developed in order to operate as fully automatic.

The SKIRON/Eta system is based on the NCEP/Eta model. A detailed description of its characteristics and configurations is to be found in Kallos (1997), Nickovic et al. (1998), Papadopoulos et al. (2002) and others.

The model has several unique capabilities making it appropriate for regional/mesoscale simulations in regions with varying physiographic characteristics. It has the unique capability to use either a "step-mountain" vertical coordinate (Mesinger 1984) or the customary pressure or sigma (or hybrid) coordinate. The SKIRON/Eta modeling system is also including dust cycle capabilities. The hydrostatic version of the system was successfully used operationally in the University of Athens since 1997, as well as in applications of simulations of historical dust-storm events (Nickovic et al. 2001). During the last years, mercury cycle modules have also been incorporated to the SKIRON/Eta system providing forecasts of the concentration and deposition of mercury in Europe and USA (Kallos et al. 2001; Voudouri et al. 2005). The main features of the system that was implemented in the Mediterranean region in the framework of MFSTEP project were described in MFSTEP-WP10 Deliverable D4. As far as subtask 10310 is concerned, a very important parameterization of SKIRON/Eta is the viscous sublayer scheme.

The viscous sublayer is a layer next to the surface which is so thin that there is no room for turbulent eddies to develop. Therefore, momentum, heat and moisture are transported through this layer by molecular diffusion. Since the molecular diffusion is much weaker than the turbulent diffusion, the presence of the viscous sublayer restricts the surface turbulent fluxes. The scheme is described in the following subsection giving special emphasis to the formulation over water surfaces.

2.1.1 Viscous sublayer

In order to calculate the surface fluxes, the similarity theory requires prescription of boundary conditions at two levels in the air, i.e., z_1 and z_2. The relevant variables at the lowest model level z_{LM} are used as the upper boundary condition. The techniques how to specify variables at the lower boundary will be described in the following paragraphs.

The profiles of the relevant atmospheric variables tend to have the log form as the lower boundary is approached. Since the log function has a singularity at $z=0$, it is usually assumed that the log profile ends at some small but finite height z_0, and that the considered variables takes on their lower boundary values at this height. This situation is illustrated in Figure 1. The height z_0 is called the roughness height or roughness length.

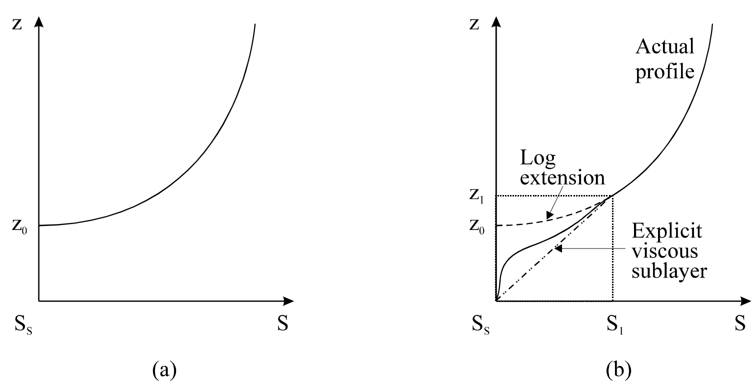

Figure 1. (a) log profile ending, and (b) log profile with the viscous sublayer ending.

The situation near the surface is however more complex than represented in Figure 1a. More realistic is the profile displayed in Figure 1b with a viscous sublayer included. This thin sublayer reflects the fact that near the surface there is no enough space for turbulent elements to develop. Different viscous sublayer approaches are applied over ground and over water surfaces. The formulation implemented over water surfaces will be described here because it is more relevant to MFSTEP project.

Viscous sublayer over water surfaces

The viscous sublayer over water surfaces is designed by matching the log profile of the considered variables with a separate viscous sublayer profile (Janjic 1994). The method specifies the height and the values of the variables at the matching point. The lower boundary values for the turbulent layer would be thus defined. Description of the method below is based on Janjic (1994, 1996).

Following Liu et al. (1979), in the immediate vicinity of a smooth surface, the profiles are assumed to be

$$U_1 - U_s = D_1\left[1 - \exp\left(-\frac{zu_*}{D_1\nu}\right)\right]\frac{M}{u_*} \tag{2.1.1}$$

$$\Theta_1 - \Theta_s = D_2\left[1 - \exp\left(-\frac{zu_*}{D_2\chi}\right)\right]\frac{H}{u_*} \tag{2.1.2}$$

$$q_1 - q_s = D_3\left[1 - \exp\left(-\frac{zu_*}{D_{31}\lambda}\right)\right]\frac{E}{u_*} \tag{2.1.3}$$

Here, the subscript s denotes the surface values, the subscript 1 denotes the values at height z_1 above the surface where the molecular diffusivities are still dominant, D_1, D_2, and D_3 are parameters to be discussed later, ν, χ and λ are the molecular diffusivities for momentum, heat and water vapor, respectively, and M, H and E are the turbulent fluxes above the viscous sublayer.

For a small argument ξ of the exponential functions in equations (2.1.1)-(2.1.3)

$$\frac{z_{1u}u_*}{D_1\nu} = \frac{z_{1T}u_*}{D_2\chi} = \frac{z_{1q}u_*}{D_3\lambda} = \xi \tag{2.1.4}$$

it can be written that

$$1 - \exp(-\xi) \approx \xi \qquad (2.1.5)$$

so that, using equations (2.1.4) and (2.1.5), equations (2.1.1)-(2.1.3) can be approximated by

$$U_1 - U_s = \frac{z_{1u}}{\nu} M \qquad (2.1.6)$$

$$\Theta_1 - \Theta_s = \frac{z_{1T}}{\chi} H \qquad (2.1.7)$$

$$q_1 - q_s = \frac{z_{1q}}{\lambda} E \qquad (2.1.8)$$

Here, the heights z_{1u}, z_{1T} and z_{1q} are defined by equation (2.1.4), i.e.

$$z_{1u} = \frac{\xi \nu D_1}{u_*} \qquad (2.1.9)$$

$$z_{1T} = \frac{\xi \chi D_2}{u_*} \qquad (2.1.10)$$

$$z_{1q} = \frac{\xi \lambda D_3}{u_*} \qquad (2.1.11)$$

At this point the following simplifying modeling assumptions are made:

There are two distinct layers: (i) a thin viscous layer immediately above the surface, where the vertical transports are determined entirely by the molecular diffusion, and (ii) a turbulent layer above it, where the vertical transports are defined entirely by the turbulent fluxes.
the depths of the viscous sublayers for the respective physical variables are defined by (2.1.9)-(2.1.11) for a chosen fixed value of ξ.

Note that with the definitions of the depths of the viscous sublayers (2.1.9)-(2.1.11), the values of the relevant physical quantities at the interfaces of the viscous and the turbulent layers are those denoted by the subscript 1 in (2.1.6)-(2.1.8).

Using the bulk momentum and heat exchange coefficients K_{Mbulk} and K_{Hbulk} respectively, the turbulent fluxes in the surface layer above the viscous sublayer are represented by

$$M = \frac{K_{Mbulk}}{\Delta z}\left(U_{lm} - U_1\right) \tag{2.1.12}$$

$$H = \frac{K_{Hbulk}}{\Delta z}\left(\Theta_{lm} - \Theta_1\right) \tag{2.1.13}$$

$$E = \frac{K_{Hbulk}}{\Delta z}\left(q_{lm} - q_1\right) \tag{2.1.14}$$

Here, the subscript *lm* denotes the variable at the lowest model level and

$$\Delta z = z_{lm} - z_1$$

where z_1 is the height of the viscous sublayer for the variable considered.

Substituting (2.1.12)-(2.1.14) into (2.1.6)-(2.1.8), one obtains

$$\frac{\nu}{z_{1u}}\left(U_1 - U_s\right) = \frac{K_{Mbulk}}{\Delta z}\left(U_{lm} - U_1\right) \tag{2.1.15}$$

$$\frac{\chi}{z_{1T}}\left(\Theta_1 - \Theta_s\right) = \frac{K_{Hbulk}}{\Delta z}\left(\Theta_{lm} - \Theta_1\right) \tag{2.1.16}$$

$$\frac{\lambda}{z_{1q}}\left(q_1 - q_s\right) = \frac{K_{Hbulk}}{\Delta z}\left(q_{lm} - q_1\right) \tag{2.1.17}$$

Note that (2.1.15)-(2.1.17) reflect the requirement for the continuity of the fluxes across the interfaces between the two layers. By solving (2.1.15)-(2.1.17) for the variables with subscript 1, one obtains

$$U_1 = \frac{U_s + \dfrac{K_{Mbulk} z_{1u}}{\nu \Delta z} U_{lm}}{1 + \dfrac{K_{Mbulk} z_{1u}}{\nu \Delta z}} \tag{2.1.18}$$

$$\Theta_1 = \frac{\Theta_s + \dfrac{K_{Hbulk} z_{1T}}{\chi \Delta z} \Theta_{lm}}{1 + \dfrac{K_{Hbulk} z_{1T}}{\chi \Delta z}} \tag{2.1.19}$$

$$q_1 = \frac{q_s + \dfrac{K_{Hbulk} z_{1q}}{\lambda \Delta z} q_{lm}}{1 + \dfrac{K_{Hbulk} z_{1q}}{\lambda \Delta z}} \tag{2.1.20}$$

Thus, the required lower boundary conditions for the turbulent layer are expressed as weighted means of the values at the surface and the lowest model level. Note that (2.1.18)-(2.1.20), together with that (2.1.9)-(2.1.11) represent a closed system provided the parameters D_1, D_2, D_3 and ξ are known.

The viscous sublayer over the ocean is assumed to operate in three different regimes: (i) smooth and transitional, (ii) rough and (iii) rough with spray, depending on the roughness Reynolds number

$$\mathrm{Re} = \frac{z_0 u_*}{\nu} \tag{2.1.21}$$

Here,

$$z_0 = \max\left(0.018 \frac{u_*^2}{g}, \quad 1.59 \times 10^{-5} \right) \tag{2.1.22}$$

When the Reynolds number exceeds a prescribed value Re_r the flow ceases to be smooth and the rough regime is entered. In the rough regime, the momentum is transported also by pressure forces on the roughness elements so that equation (2.1.1) looses validity. Consequently, the viscous sublayer for momentum is turned off. However, for heat and moisture the viscous sublayer is still operating until the rough regime with spray is reached at a critical value Re_s when the viscous layer collapses completely. In the rough regime with spray the breaking waves and the spray are assumed to provide much more efficient way of exchange of heat and moisture between the ocean and the air than that can be accomplished by the molecular viscosity. Note that instead in terms of Re, the boundaries between the regimes can be expressed in terms of u_*, since Re is a monotonic function of u_*.

For the parameters D_1, D_2, and D_3 Liu et al. (1979) suggest

$$D_1 = G\,\mathrm{Re}^{1/4} \tag{2.1.23}$$

$$D_2 = G\,\mathrm{Re}^{1/4}\ \mathrm{Pr}^{1/2} \tag{2.1.24}$$

$$D_3 = G\,\mathrm{Re}^{1/4}\ Sc^{1/2} \tag{2.1.25}$$

where $\mathrm{Pr} = \dfrac{\nu}{\chi}$ is the Prandtl number, $Sc = \dfrac{\nu}{\lambda}$ is the Schmidt number, and G is a constant depending on flow regimes.

With these definitions, and the definition (2.1.21), equations (2.1.9)-(2.1.11) take the form

$$z_{1u} = \xi\nu \frac{G\left(\dfrac{z_0 u_*}{\nu}\right)^{1/4}}{u_*} \tag{2.1.26}$$

$$z_{1T} = \xi\chi \frac{G\left(\dfrac{z_0 u_*}{\nu}\right)^{1/4} \mathrm{Pr}^{1/2}}{u_*} \tag{2.1.27}$$

$$z_{1q} = \xi\lambda \frac{G\left(\frac{z_0 u_*}{\nu}\right)^{1/4} Sc^{1/2}}{u_*} \quad (2.1.28)$$

In SKIRON/Eta model, $G = 30$ is used for the smooth regime, following Liu et al. (1979). When the flow ceases to be smooth, $G = 10$ is applied, which fits well with the data of Mangarella et al. (1973). The Prandtl number and the Schmidt number are assumed to be the same, i.e., $Pr = Sc = 0.71$, and the molecular viscosity for momentum is $\nu = 0.000015$.

The threshold velocities at which the transition between different flow regimes occur are $u_{*r} = 0.025ms^{-1}$ and $u_{*s} = 0.70ms^{-1}$. The value of $\xi = 0.35$ is used.

In the practical implementation, u_* is calculated as

$$u_* = \sqrt{\frac{K_{Mbulk}}{\Delta z}\left(U_{lm} - U_1\right)}$$

using K_{Mbulk} and U_1 from the previous time step. Then, u_* is used in (2.1.22) to update z_0. With z_{1u}, z_{1T}, and z_{1q} being calculated from (2.1.26)-(2.1.28), the lower boundary conditions U_1, T_1, and q_1 are specified from (2.1.18)-(2.1.20) using K_{Mbulk} and K_{Hbulk} from the previous time step. In order to prevent the two-grid-interval oscillation in time, the average values of U_1, T_1, and q_1 from the present and the previous time step are used.

2.2 NCEP/Eta hydrostatic model

The NCEP/Eta model used in ICoD's experiments belongs to the same generation of the model as the SKIRON/Eta, described in details in the MFSTEP-WP10 Deliverable Report D4.

2.3 NCEP/NMM nonhydrostatic model

General. Within the WRF (Weather Research and Forecasting) initiative in the USA, a new approach at NCEP has been applied in developing the nonhydrostatic model NMM (Janjic et al., 2001, Janjic, 2003). Namely, instead of extending the cloud model concepts to synoptic scales and beyond, the hydrostatic approximation is relaxed in a hydrostatic model formulation. In this way the validity of the model dynamics is extended to non-hydrostatic motions, the number of prognostic equations remains the same as in the hydrostatic model, and at the same time the favorable features of the hydrostatic formulation are preserved. In high-resolution numerical weather prediction applications, the efficiency of the computational algorithm applied in the NMM significantly exceeds the efficiency of the algorithms used in several established state-of-the-art non-hydrostatic models. The high computational efficiency of the NMM has been achieved primarily due to the design of the time-stepping procedure, and due to the choice of the horizontal grid. The high computational efficiency of the NMM demonstrates that meaningful non-hydrostatic forecasting/simulations are rapidly becoming feasible at smaller centers also, using workstations and PC's. The description below is based on the Janjic (2003) article. This approach is based on relaxing the hydrostatic approximation in a hydrostatic model using vertical coordinate based on hydrostatic pressure. In this way the applicability of the model was extended to the nonhydrostatic motions. In order to do so, the system of nonhydrostatic equations was split into two parts: (a) the part that corresponds to the hydrostatic system, except for higher order corrections due to the vertical acceleration, and (b) the system of equations that allows computation of the corrections appearing in the first system due to vertical acceleration. The separation of the nonhydrostatic contributions shows in a transparent way that the hydrostatic approximation affects the equations. The described procedure does not require any linearization or approximation. At the same time, the favorable features of the hydrostatic model are preserved within the range of validity of the hydrostatic approximation. The nonhydrostatic dynamics has been introduced through an add–on module in the NCEP Meso (“Eta”) model (Janjic et al., 2001). The nonhydrostatic module can be turned on and off depending on resolution. This allows easy comparison of hydrostatic and nonhydrostatic solutions obtained using otherwise identical model.

Governing equations. For simplicity, as a representative of mass based vertical coordinates, consider the sigma vertical coordinate

$$\sigma = \frac{(\pi - \pi_t)}{\mu}, \tag{2.3.1}$$

where π is the hydrostatic pressure, and μ represents the difference in hydrostatic pressure between the base and top of the model column; i.e.

$$\mu = \pi_s - \pi_t . \tag{2.3.2}$$

Here, π_s and π_t stand for the hydrostatic pressures at the surface and at the top of the model atmosphere. Then, the equations governing a dry, inviscid and adiabatic nonhydrostatic atmosphere are (Janjic et al., 2001)

$$\frac{\partial \mu}{\partial t} = -\int_0^1 \nabla_\sigma \bullet (\mu \mathbf{v}) d\sigma' , \tag{2.3.3}$$

$$p\alpha = RT , \tag{2.3.4}$$

$$\Phi = \Phi_s + \mu \int_\sigma^1 \frac{RT}{p} d\sigma . \tag{2.3.5}$$

$$\frac{d\mathbf{v}}{dt} = -(1+\varepsilon)\nabla_\sigma \Phi - \alpha \nabla_\sigma p + f\mathbf{k} \times \mathbf{v} , \tag{2.3.6}$$

$$\frac{\partial T}{\partial t} = -\mathbf{v} \bullet \nabla_\sigma T - \dot{\sigma}\frac{\partial T}{\partial \sigma} + \frac{\alpha}{c_p}[\mathbf{v} \bullet \nabla_\sigma p - (1+\varepsilon)\int_0^\sigma \nabla_\sigma \bullet (\mu \mathbf{v}) d\sigma'] + \frac{\alpha}{c_p}[\frac{\partial p}{\partial t} - (1+\varepsilon)\frac{\partial \pi}{\partial t}] , \tag{2.3.7}$$

$$\frac{\partial p}{\partial \pi} = 1 + \varepsilon , \tag{2.3.8}$$

$$w = \frac{1}{g}\frac{d\Phi}{dt} = \frac{1}{g}\Big(\frac{\partial \Phi}{\partial t} + \mathbf{v} \bullet \nabla_\sigma \Phi + \dot{\sigma}\frac{\partial \Phi}{\partial \sigma}\Big) , \tag{2.3.9}$$

$$\varepsilon = \frac{1}{g}\frac{dw}{dt} = \frac{1}{g}\Big(\frac{\partial w}{\partial t} + \mathbf{v} \bullet \nabla_\sigma w + \dot{\sigma}\frac{\partial w}{\partial \sigma}\Big) . \tag{2.3.10}$$

Here, in the order of appearance, $\mathbf{v}$ is the horizontal wind vector, p is the actual, nonhydrostatic pressure, R is the gas constant for dry air, T is temperature, Φ is geopotential and Φ_S is the geopotential of the Earth's surface. The other symbols used have either their usual meaning, or their meaning is self-evident. Note that the nonhydrostatic continuity equation (2.3.9), and the definition of ε (2.3.10), are not independent equations. The parameter ε is the central point of the extended, nonhydrostatic dynamics. As can be readily verified, if ε is zero, (2.3.3)-(2.3.7) reduce to the familiar, hydrostatic equations. The additional equations (2.3.8)-(2.3.10) are needed in order to compute the corrections due to nonzero ε. On the synoptic scales, ε is small and approaches the computer round–off error. In case of vigorous convective storms, or strong vertical accelerations in the flows over steep obstacles, ε can reach the order of 10^{-3}.

Horizontal differencing. The NCEP/NMM and NCEP/Eta use the same type of the semi-staggered E horizontal grid. According to studies of Winninghoff (1968) and Arakawa and Lamb (1977), compared to other grids considered, generally better agreement with the exact frequencies was obtained on the staggered grid C, and on the semi-staggered grid B (or E). These considerations, however, do not give decisive advantage to either of the two choices. The problems on the semi-staggered grids B and E are restricted mainly to the shortest waves, while in the case of the slow internal modes, and/or weak stability, the C grid may develop problems in the entire range of the admissible wave numbers (Arakawa and Lamb, 1977). In addition, there is an effective technique for filtering the low frequency, short-wave noise resulting from the inaccurate computation of the divergence term on the semi-staggered grids (Janjic, 1979). More sophisticated, nondissipative methods ("deaveraging" and "isotropisation") for dealing with the problem have been also proposed (Janjic et al., 1998), leading to dramatic improvements of the finite-difference frequencies of the short gravity-inertia waves on the semi-staggered grids, particularly important for the nonhydrostatic dynamics.

Vertical coordinate and topography. The operational version of the NCEP hydrostatic Meso ("Eta") model uses a step-like representation of mountains originally proposed by Bryan (1969) in the z vertical coordinate. This approach was modified for a sigma coordinate model by Mesinger et al. (1988). The advantage of the step-like mountain representation is that the coordinate surfaces are quasi-horizontal. This, however, is not without consequences. For example, internal discontinuities are introduced at the vertical sides of the steps that replace the mountain slopes, and lateral boundary conditions are required at these discontinuities. The formal accuracy of the finite-differences at the points next to the internal boundaries is reduced to the first order. In addition to that, if the no slip boundary conditions are used in order to preserve in a simple way the major favorable features of the finite-differencing schemes (Janjic, 1977, 1979, 1984), a nonphysical sink of momentum is introduced. Yet another problem is the representation of the physical processes in the surface layer and the planetary boundary layer (PBL). The vertical resolution needed for adequate treatment of the PBL should be rather fine. This was one of the major problems in the process of developing the physical package for the Meso ("Eta") model (Janjic, 1990, 1994). However, with the increasing computing power and model resolutions, several problems that could be associated with the step-mountain representation of topography started to surface up, particularly at smaller scales, and in mountainous areas. For example, the model using the step-mountain representation failed to reproduce a catabatic windstorm in the Rockies, while the forecast using the conventional sigma coordinate was quite successful in this respect (Janjic and DiMego, 2001). In addition, several recent studies (Adcroft et al, 1997; Galus, 2000, Gallus and Klemp, 2000, Janjic and DiMego, 2001) indicate that more problems should be expected at even higher resolutions. Another problem possibly related to the mountain representation is that the NCEP operational Meso model using the step-mountains is producing precipitation too far down on the slopes of major orographic obstacles (Staudenmeier and Mittelstadt, 1998). In response to the step-mountain problems, in the nonhydrostatic Meso model the conventional σ coordinate terrain-following representation of mountains has been used in most tests so far. Recently, the hybrid pressure-sigma vertical coordinate option has been introduced (Arakawa and Lamb, 1977). With the hybrid coordinate, the coordinate surfaces are flat above and away from the mountains. In the vicinity of the mountains the hybrid coordinate has increased vertical resolution, and the equations are continuous, without the computational internal boundary conditions that have to be specified with the step-mountains. The sloping coordinate surfaces in the vicinity of the mountains, and the related inaccuracies, are the price to pay for these benefits. The usual, Lorenz vertical staggering of the variables is used in the vertical. The geopotential and the nonhydrostatic pressure are defined at the interfaces of the layers, while all three velocity components and temperature are carried in the middle of the model layers. The vertical velocity is defined at the E grid mass points.

Time differencing. In the NCEP hydrostatic Meso ("Eta") model additive time splitting is used. The hydrostatic system of equations is split into the following two subsystems

$$\left(\frac{\partial \mathbf{v}}{\partial t}\right)_i = -\nabla_\sigma \Phi - \alpha \nabla_\sigma \pi + f\mathbf{k}\times\mathbf{v} \tag{2.3.11}$$

$$\left(\frac{\partial T}{\partial t}\right)_i = \frac{\alpha}{c_p}[\mathbf{v}\cdot\nabla_\sigma \pi - \int_0^\sigma \nabla_\sigma \cdot (\mu\mathbf{v})\, d\sigma'] \tag{2.3.12}$$

$$(\frac{\partial \mu}{\partial t})_i + \nabla_\sigma \cdot (\mu \mathbf{v}) + \frac{\partial(\mu\dot{\sigma})}{\partial \sigma} = 0 \qquad (2.3.13)$$

$$(\frac{\partial \mathbf{v}}{\partial t})_{ii} = -\mathbf{v}\nabla_\sigma \mathbf{v} - \dot{\sigma}\frac{\partial \mathbf{v}}{\partial \sigma} \qquad (2.3.14)$$

$$(\frac{\partial T}{\partial t})_{ii} = -\mathbf{v}\cdot\nabla_\sigma T - \dot{\sigma}\frac{\partial T}{\partial \sigma} \qquad (2.3.15)$$

The time derivatives of the two subsystems are denoted by subscripts *i* and *ii*, respectively. The system (2.3.11)-(2.3.13) is solved using short time steps, and the system (2.3.14)-(2.3.15) is solved using long time steps. The system (2.3.11)–(2.3.13) conserves energy. The system (2.3.14)–(2.3.15) also conserves energy, except for the changes due to the redistribution of mass. An economical forward–backward scheme (Ames, 1969; Gadd, 1974) with the trapezoidal scheme for the Coriolis term (Janjic and Wiin–Nielsen, 1977) has been used for the system (2.3.11)–(2.3.13) (Janjic, 1979). Concerning the contributions of the advection terms (2.3.14)–(2.3.15), the two–step iterative Adams–Bashforth scheme is used. The Adams–Bashforth scheme allows about the same computational efficiency as the two–step, iterative scheme with twice longer time steps. The Adams-Bashforth scheme has also been used for the Coriolis force terms. Another recent novelty is that the iterative method for solving the vertical implicit pressure equation discussed in Janjic et al. (2001) has been replaced by direct solver. This modification has brought a visible improvement in the computational efficiency of the model.

3 Experimental setup

3.1 IASA

The viscous sublayer scheme was evaluated by a series of experiments in which the scheme was turned off. IASA produced 72-hour hindcasts initialized from the daily 0000 UTC ARPEGE analyses of January 2003 (SVP period). The corresponding ARPEGE forecasts were used as lateral boundary conditions at 3-hourly time intervals. 31 simulations (without the viscous sublayer scheme) became available for the evaluation of the scheme. Finally, the above model outputs were compared with the SVP results.

More specifically, IASA performed the following two groups of experiments:

A. SKIRON/Eta runs with the viscous sublayer scheme (SVP runs), and

B. SKIRON/Eta runs without the viscous sublayer scheme.

The model setup was the one used during SVP, pre-TOP and TOP periods. It is reminded that the horizontal resolution was 0.1°x0.1° (latitude-longitude) and 38 model layers were used in the vertical, ranging from the surface up to 25 hPa. The variables at the lowest model layer were calculated at a height of 10m above sea points.

3.2 ICoD

ICoD performed the following three groups of experiments:

A. NCEP/Eta model runs (Experiment *'ETA.visc.yes'*), belonging to the same model generation as SKIRON/Eta; the model was run with the viscous sublayer

B. NCEP/NMM model runs (Experiment *'NMM.visc.yes'*), with the viscous sublayer, and

C. NCEP/NMM model runs(Experiment *'NMM.visc.no'*), without the viscous sublayer

All model versions were executed over the period of 1-31 January 2005 in a sequence of 24-hour simulation runs. The initial and boundary conditions were specified using the Meteo-France 00Z analyses with 0.25 deg horizontal resolution and with 3 hours time interval. The domain of the models was as shown in the figures of the next section. A, B, and C experiments were run with approx. 0.1 deg horizontal resolution of the rotated latitude-longitude grid, and with 24 model layers in the vertical, ranging from the surface up to 100 hPa. The height of the lowest model level carrying wind, moisture and temperature variables was 80m above sea points.

In the post-processing part, the models variables were interpolated from the model vertical coordinate into 10 standard pressure levels. In the horizontal, variables were interpolated to the agreed Project validation area: 29N-48N; 11W-42E, with 0.1 deg resolution. The near-surface variables and a selection of the upper-air model variables were archived in the GRIB format for the purpose of the subsequent models validation.

4 Results

The experiments described in Section 3 were performed in order to explore the sensitivity of the Mediterranean atmospheric circulation over the sea on different modelling conditions. In the experiments of ICoD, *'ETA.visc.yes'* was used as a reference run providing simulations with the NCEP/Eta hydrostatic model that is used by numerous groups in the Mediterranean region. The most recent version of the nonhydrostatic NCEP/NMM was used for two-fold purposes: a) to compare results with the Experiment A, and b) to explore influence of the viscous sublayer approach on near-surface atmospheric conditions over the marine environment.

This kind of study could indicate possible impacts of different surface flux calculations on ocean model forcing responses. A basis of our analysis and conclusions are results of simulations performed over the MFSTEP/SVP period of 1-31 January 2003. The viscous sublayer was introduced as reaction to the fact that predicted surface fluxes by the NCEP/ETA model as noticed by NCEP in 90s were unrealistically high over the ocean. Thus, we may in general expect that fluxes based on the viscous sublayer model should get lower values in our experiments. However, the nonlinear character of the atmospheric processes and their complex interactions (affecting fluxes) may establish links between fluxes and viscous effects which are not as simple as anticipated.

January 2003 atmospheric conditions were characterized by fast-moving low-pressure systems. Daily mean-sea-level pressure analysis charts valid at 0000 UTC are presented in the APPENDIX to illustrate variability of surface atmospheric circulation. Such dynamic variability based on short-living cyclones is generally typical for winter weather conditions in the Mediterranean. Only during 14, 15, 16, 20, and 21 January, the Mediterranean region was affected by high-pressure anticyclone circulation.

Figures 2 shows simulated monthly means of 850hPa geopotential height in *'ETA.visc.yes'* and *'NMM.visc.yes'* experiments. As can be noticed, differences become more negligible in the lower troposphere above the boundary layer.

Both monthly MSL pressure maps evaluated from the *'ETA.visc.yes'* and *'NMM.visc.yes'* experiments (Figure 3) generate a low-pressure structure in the central-northern part of the Mediterranean and anticyclonic conditions in the western Mediterranean. *'ETA.visc.yes'* produces approx. ~2 hPa deeper pressure in the 'mean' cyclone over the Adriatic Sea than *'NMM.visc.yes'*.

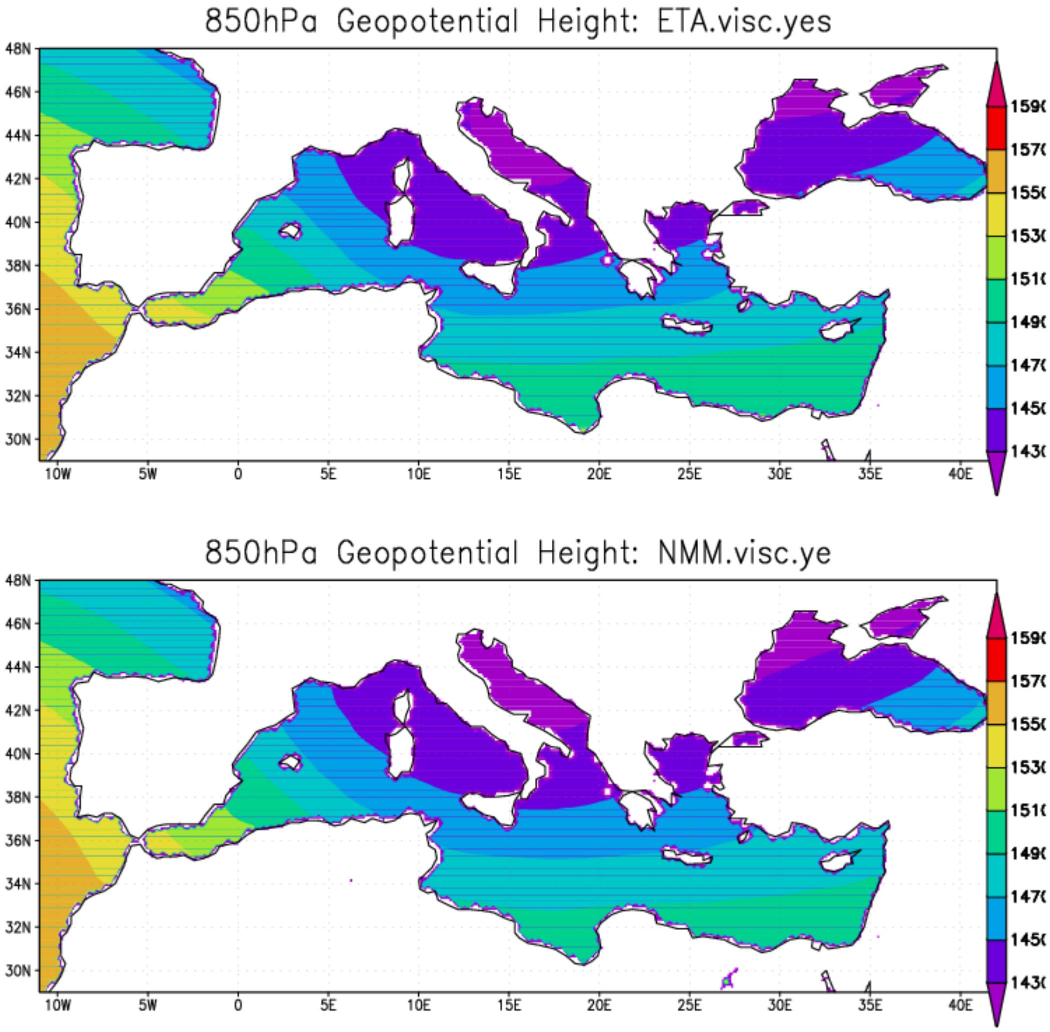

Figure 2. Simulated monthly means of 850 hPa geopotential height valid at 12:00 UTC in the *ETA.visc.yes* (upper panel) and *NMM.visc.yes* (lower panel) experiments

There are various possible reasons for such differences (also noticed and later shown for other considered parameters). NCEP/ETA and NCEP/NMM have in general the same numerical formulations for the horizontal advection, hydrostatic pressure gradient force, turbulence, large-scale and convective precipitation and lateral diffusion terms. However, the two modeling systems substantially differ in the treatment of topographic influence by using different formulations of the vertical coordinate systems. In addition, NMM has incorporated nonhydrostatic dynamics and novel formulations in the time-differencing schemes. Within NMM, ICoD made a quick experiment testing how much hydro- and nonhydrostatic options affect the model results. It was found that with the horizontal resolution of 0.1 deg used in the experiments marginal differences appear in most of the parameters (not shown). Some previous experiences indicated that larger differences could be expected if atmospheric scales smaller than ~3km were resolved.

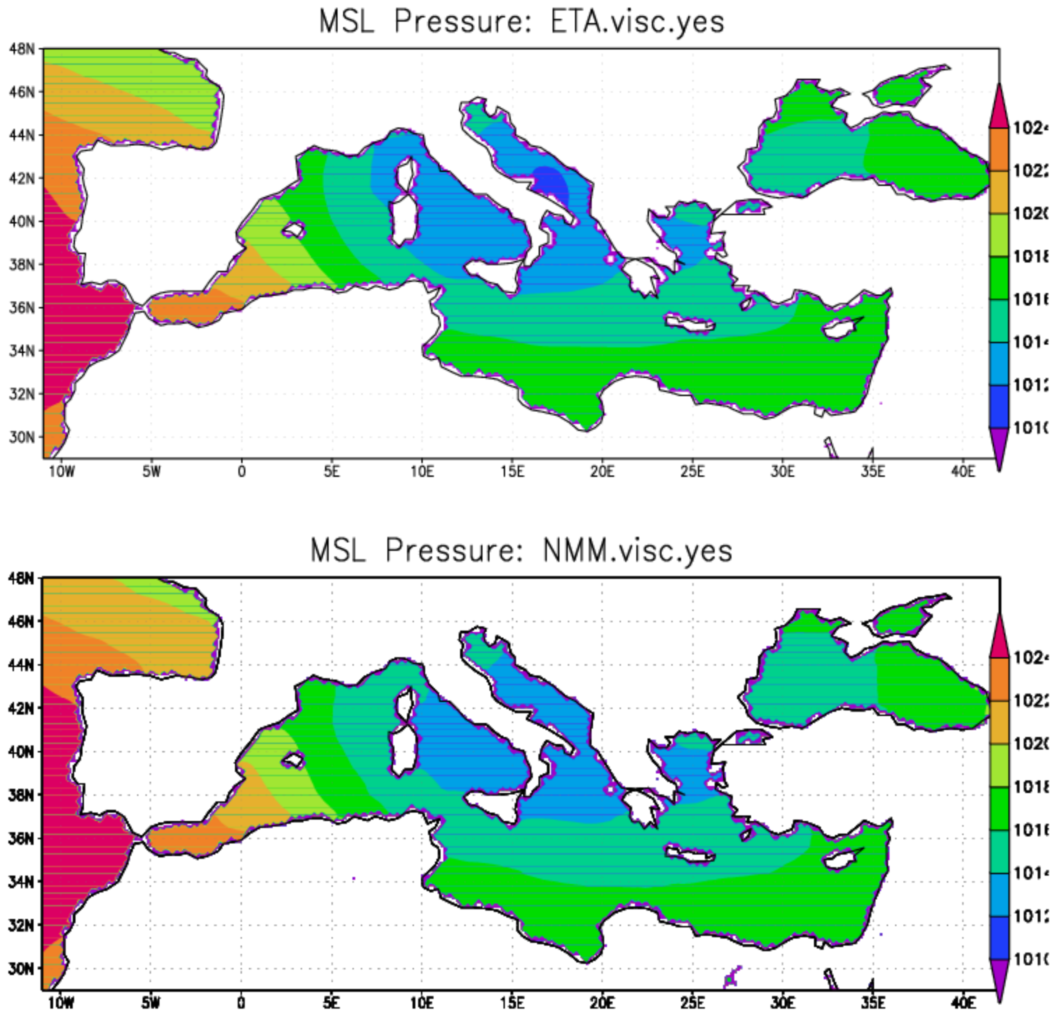

Figure 3. Simulated monthly means of MSL pressure valid at 12:00 UTC in the *ETA.visc.yes* (upper panel) and *NMM.visc.yes* (lower panel) experiments

Figures 4 and 5 show simulated monthly means of 10m-wind intensity and 2m temperatures in the *'ETA.visc.yes'* and *'NMM.visc.yes'* experiments, respectively. In general, stronger 10m wind speed is simulated by the Eta model, in particular in the eastern and central-southern

Mediterranean. Concerning the 2m temperatures, NMM.visc.yes simulates colder near-surface conditions than *ETA.visc.yes*.

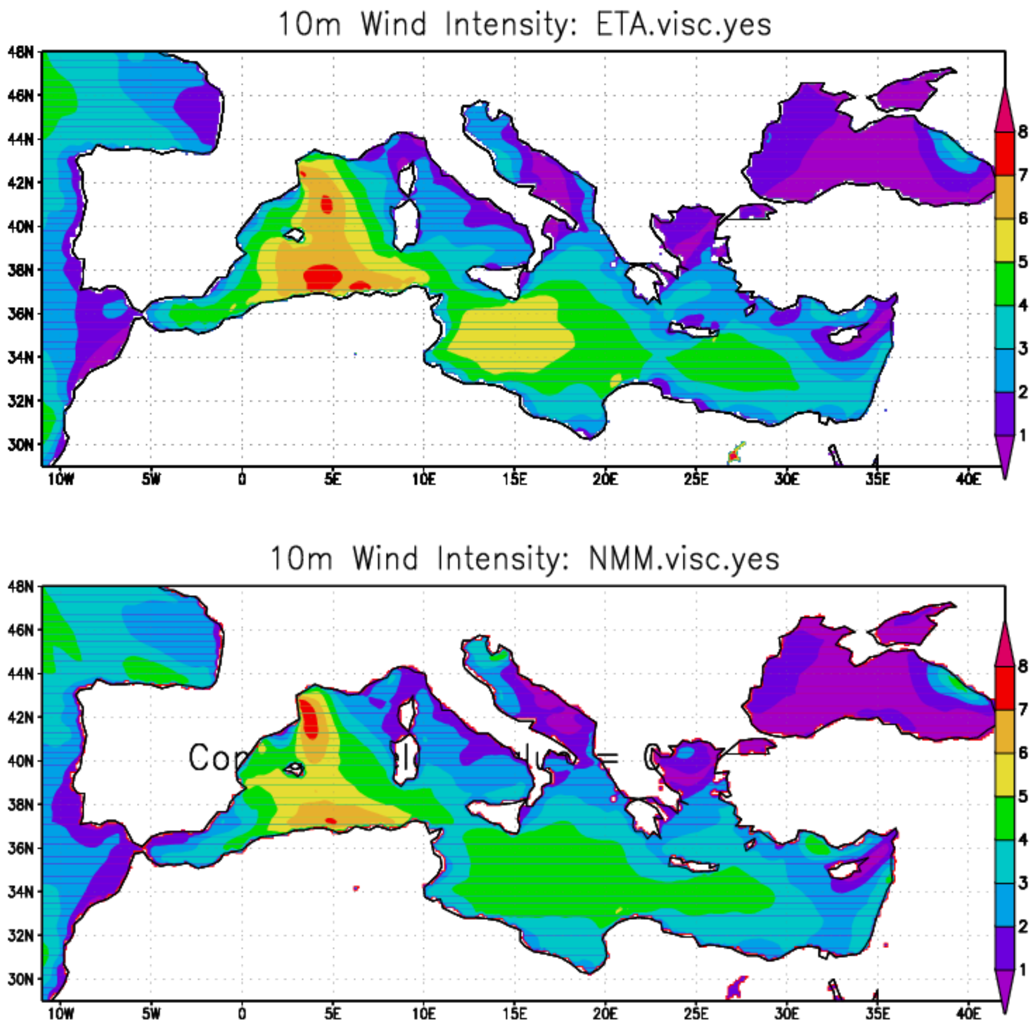

Figure 4. Simulated monthly means of 10m-wind intensity valid at 12:00 UTC in the *ETA.visc.yes* (upper panel) and *NMM.visc.yes* (lower panel) experiments

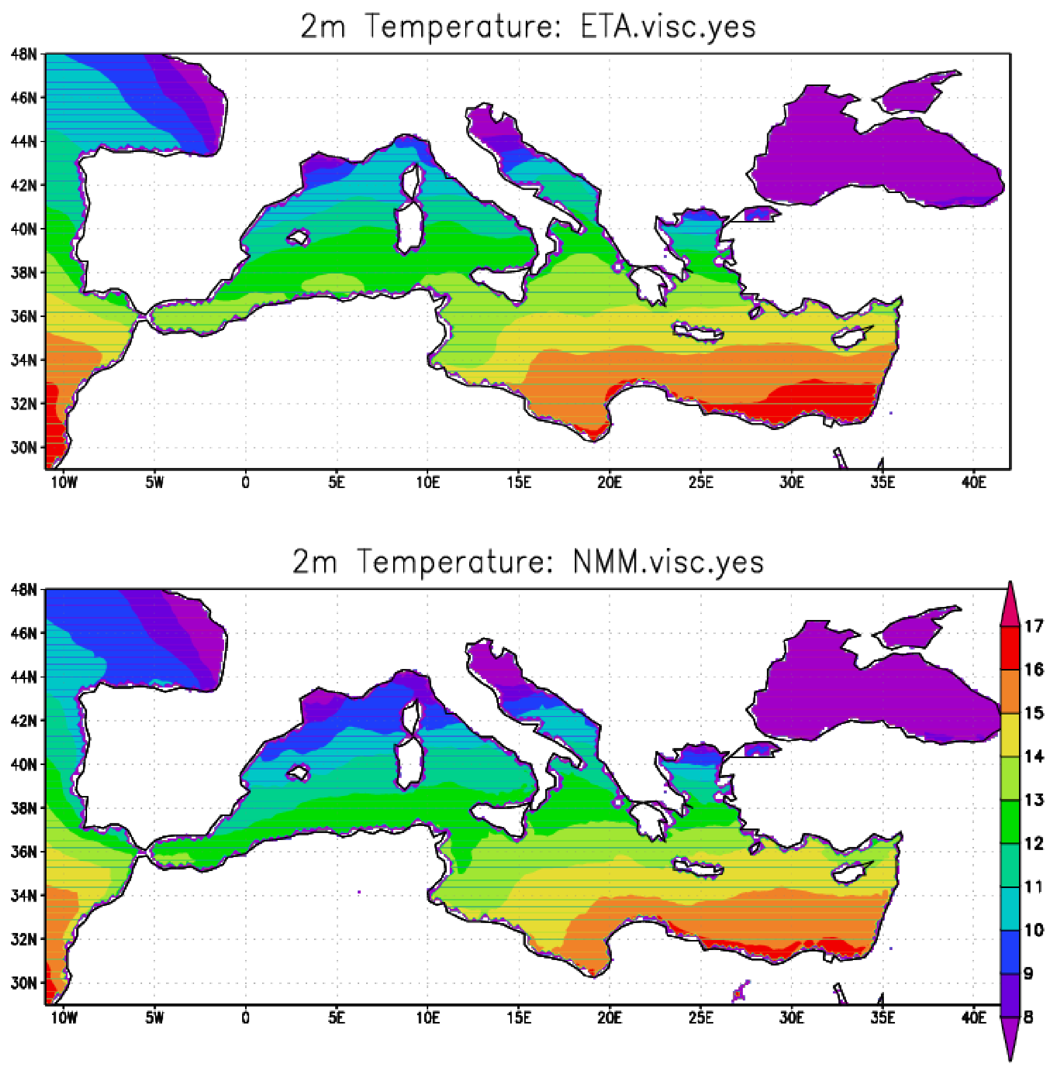

Figure 5. Simulated monthly means of 2m temperature valid at 12:00 UTC in the *ETA.visc.yes* (upper panel) and *NMM.visc.yes* (lower panel) experiments

In the following figures, differences between various parameters in *NMM.visc.yes* and *ETA.visc.yes* tests are shown in order to indicate how much the choice of the model affects the simulation of near-surface conditions over the sea. The differences a) between *NMM.visc.yes* and *NMM.visc.no* and b) between the SKIRON/Eta runs with and without the viscous sublayer are also presented in order to illustrate the influence of the viscous sublayer calculations. Figure 6 shows the differences in the 10m wind intensity in the NCEP/ETA and NCEP/NMM experiments. As can be noticed, differences range from $-2.2ms^{-1}$ to $2ms^{-1}$ with general tendency of *ETA.visc.yes* to produce slightly stronger winds in a larger part of the Mediterranean basin. The

10m wind differences indicate the prediction of weaker winds in the largest part of the domain, except in the central Mediterranean, when the viscous sublayer is included in NMM. Figure 7 shows the monthly-mean 10m wind speed differences between the SKIRON/Eta experiments with and without the viscous sublayer in January 2003. The average field has been calculated using hourly forecasts. Similarly to NMM, SKIRON/Eta predicts stronger 10m winds in the largest part of the Mediterranean basin when the viscous sublayer scheme is not included. However, in SKIRON/Eta the use of the viscous sublayer results to stronger 10m winds mainly in Eastern Mediterranean and the Black Sea and not in Central Mediterranean. In the SKIRON/Eta and the NMM experiments the monthly-mean differences range from -0.2 m/s to 0.15 m/s.

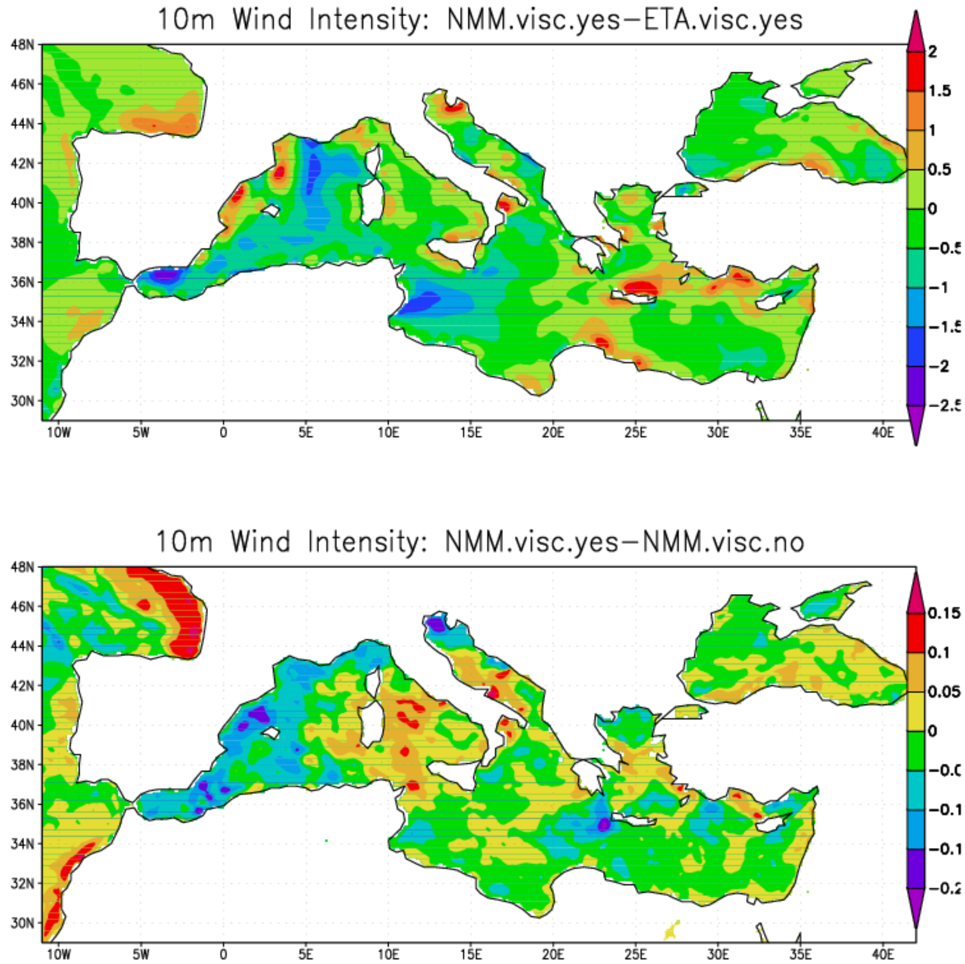

Figure 6. Simulated monthly means of 10m-wind intensity differences valid at 12:00 UTC in the *NMM.visc.yes-ETA.visc.yes* (upper panel) and *NMM.visc.yes-NMM.visc.no* (lower panel) experiments

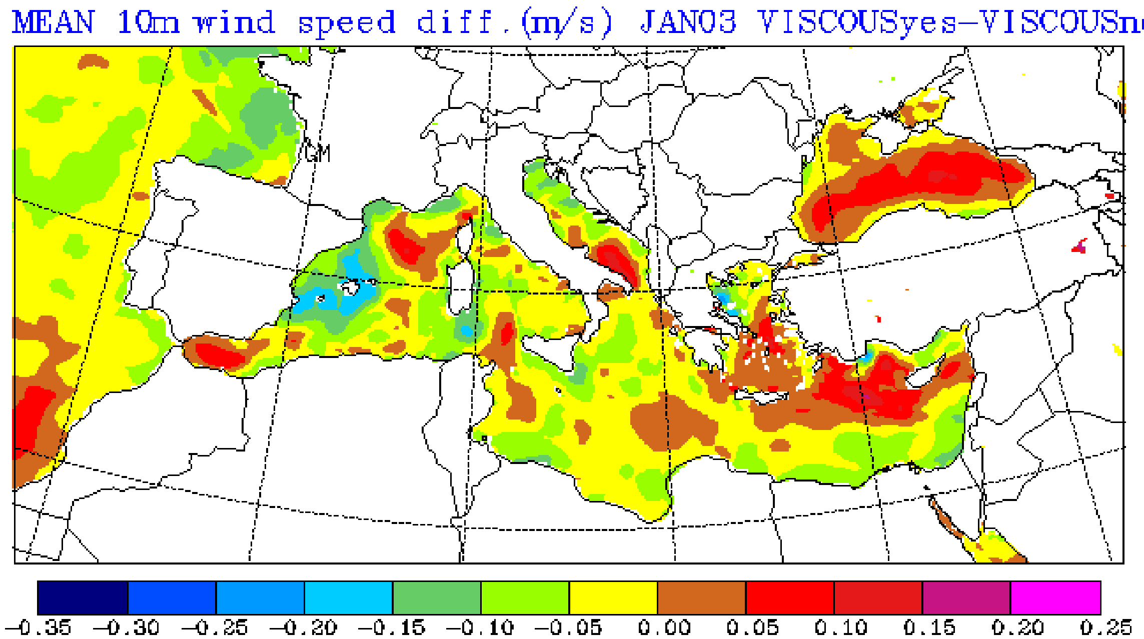

Figure 7. Monthly-mean 10m wind speed differences between the SKIRON/Eta runs with and without the viscous sublayer in January 2003. Units: m/s. Positive values indicate the prediction of stronger 10m winds when the viscous sublayer scheme is included.

Surface turbulent coefficients K_H and K_M for moisture/heat and momentum, directly influence calculation of fluxes at the air-sea interface (having also other contributions on e.g. vertical gradients of moisture and temperature). Differences in K_H (K_M is not shown, being with similar patterns as K_H) indicate that *NMM.visc.yes* has less turbulent mixing than *ETA.visc.yes* in a larger part of the domain (except along coastlines) (Figure 8).

In agreement with theory, SKIRON/Eta predicted stronger latent and sensible fluxes from the sea-surface to the atmosphere when the viscous sublayer scheme was not included (Figure 9). The largest differences appeared in the moisture fluxes in the western Mediterranean where they exceeded 20-30 W/m^2 in large regions. It is noteworthy, that the use of the viscous sublayer scheme resulted to stronger mean fluxes only in the southern Black Sea and in a number of areas near the coastline. These results show that the surface fluxes are influenced by nonlinear processes and complex interactions that need further investigation.

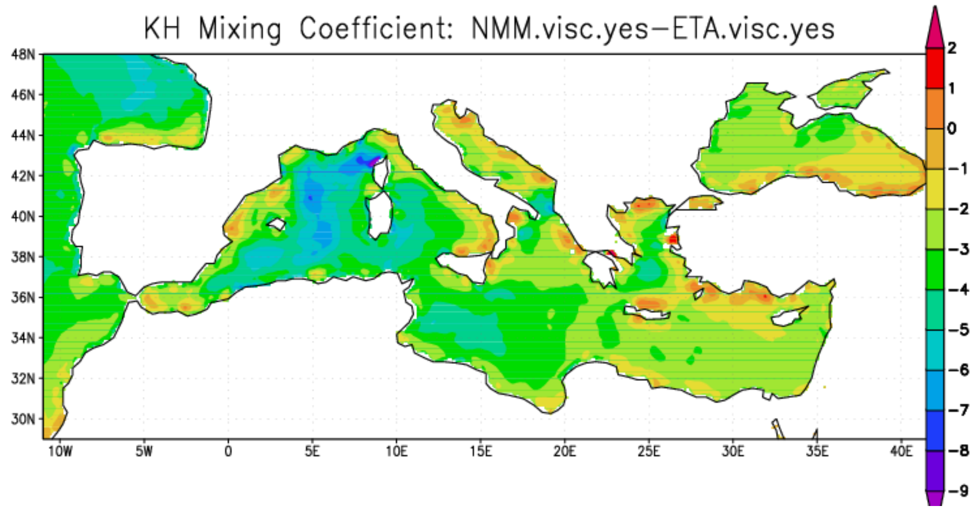

Figure 8. Simulated monthly means of turbulent mixing coefficient K_H ($100m^2s^{-1}$) valid at 12:00 UTC in the *NMM.visc.yes-ETA.visc.yes* experiments.

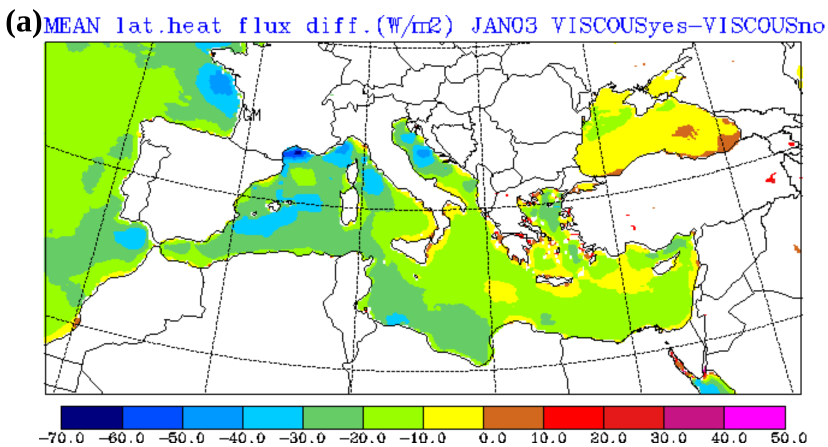

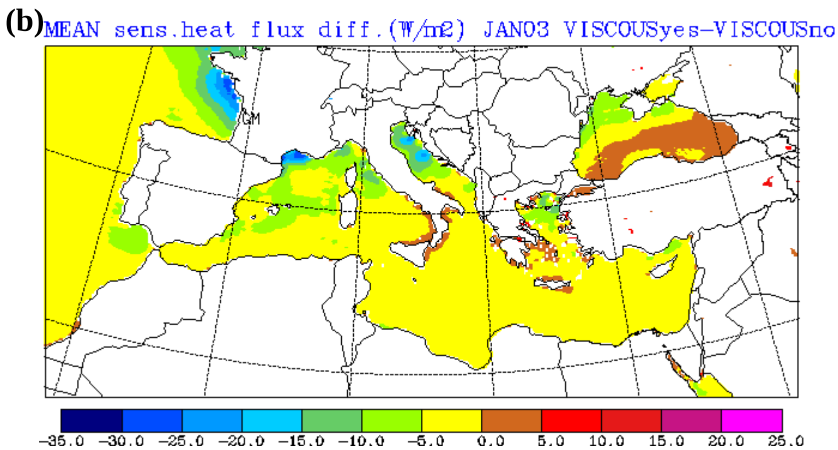

Figure 9. Monthly-mean differences of a) surface latent heat flux and b) surface sensible heat flux between the SKIRON/Eta runs with and without the viscous sublayer in January 2003. Units: W/m^2. Positive values indicate the prediction of stronger upward fluxes when the viscous sublayer scheme is included.

The total incoming long-wave radiation shows small relative differences between the two NMM experiments (Figure 10), although in *NMM.visc.yes* the larger part of the Mediterranean Sea receives less long-wave energy from the atmosphere.

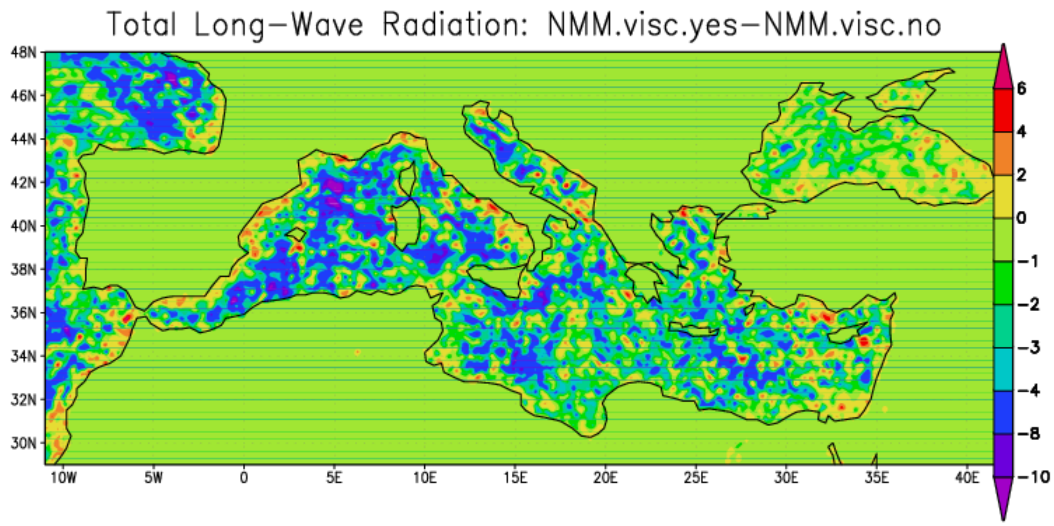

Figure 10. Simulated monthly means total incoming long-wave radiation (Wm^{-2}) valid at 12:00 UTC in the *NMM.visc.yes- NMM.visc.no* experiment

The comparison of the total incoming short-wave radiation in *ETA.visc.yes* and *NMM.visc.yes* (Figure 11) systematically shows higher values to be obtained from the NCEP/Eta experiments in the largest part of the domain. The same result shown in a different way is displayed in Figure 12, upper panel. However, differences between the two NCEP/NMM groups of experiments are such that *NMM.visc.yes* generates ~10% more short-wave energy (Figure 12, lower panel). Similarly, SKIRON/Eta predicts stronger incoming short-wave radiation when the viscous sublayer scheme is included (Figure 13). These results indicate that SKIRON/Eta and NCEP/NMM models simulate larger cloud cover amounts when the viscous sublayer scheme is not included, reducing the shortwave radiation that finally reaches the surface of the earth.

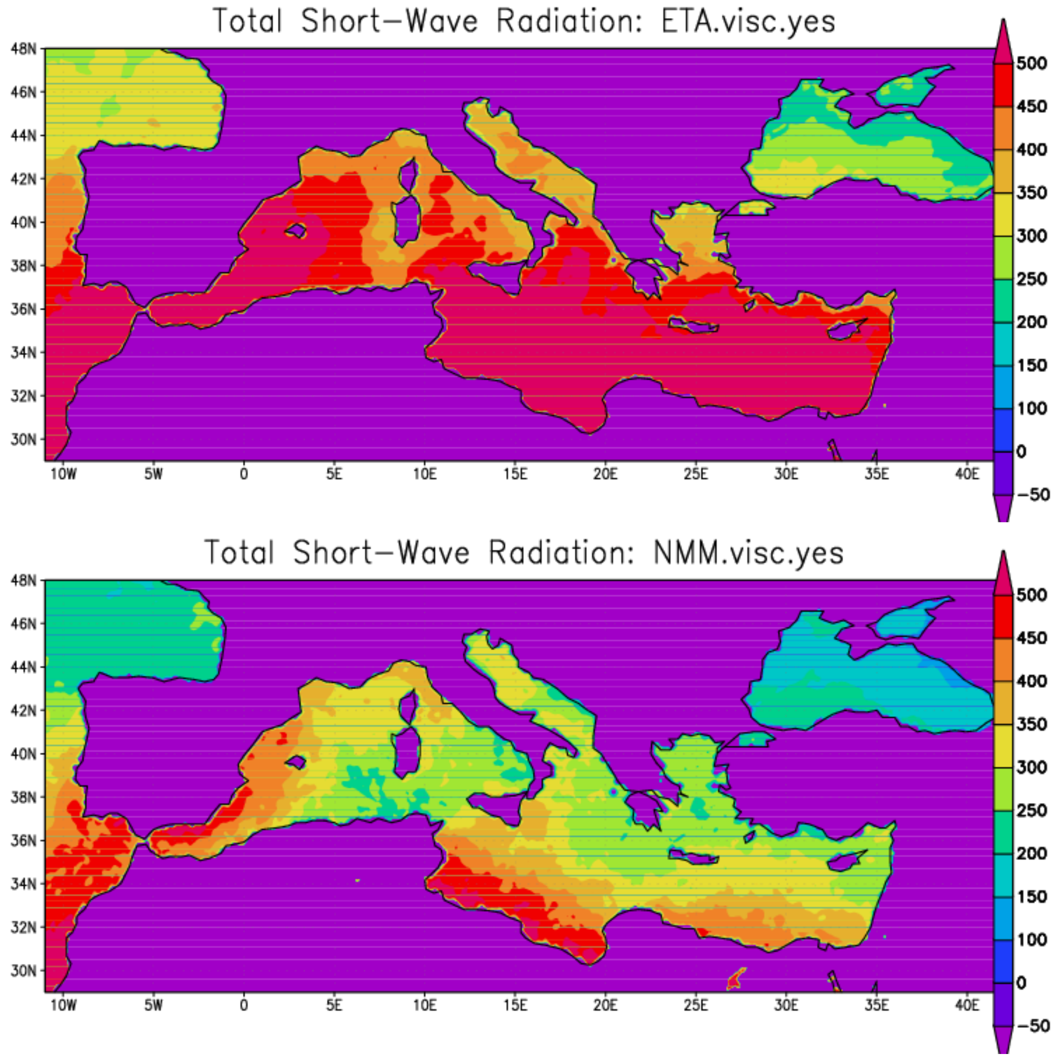

Figure 11. Simulated monthly total incoming short-wave radiation valid at 12:00 UTC in the *ETA.visc.yes* (upper panel) and *NMM.visc.yes* (lower panel) experiments

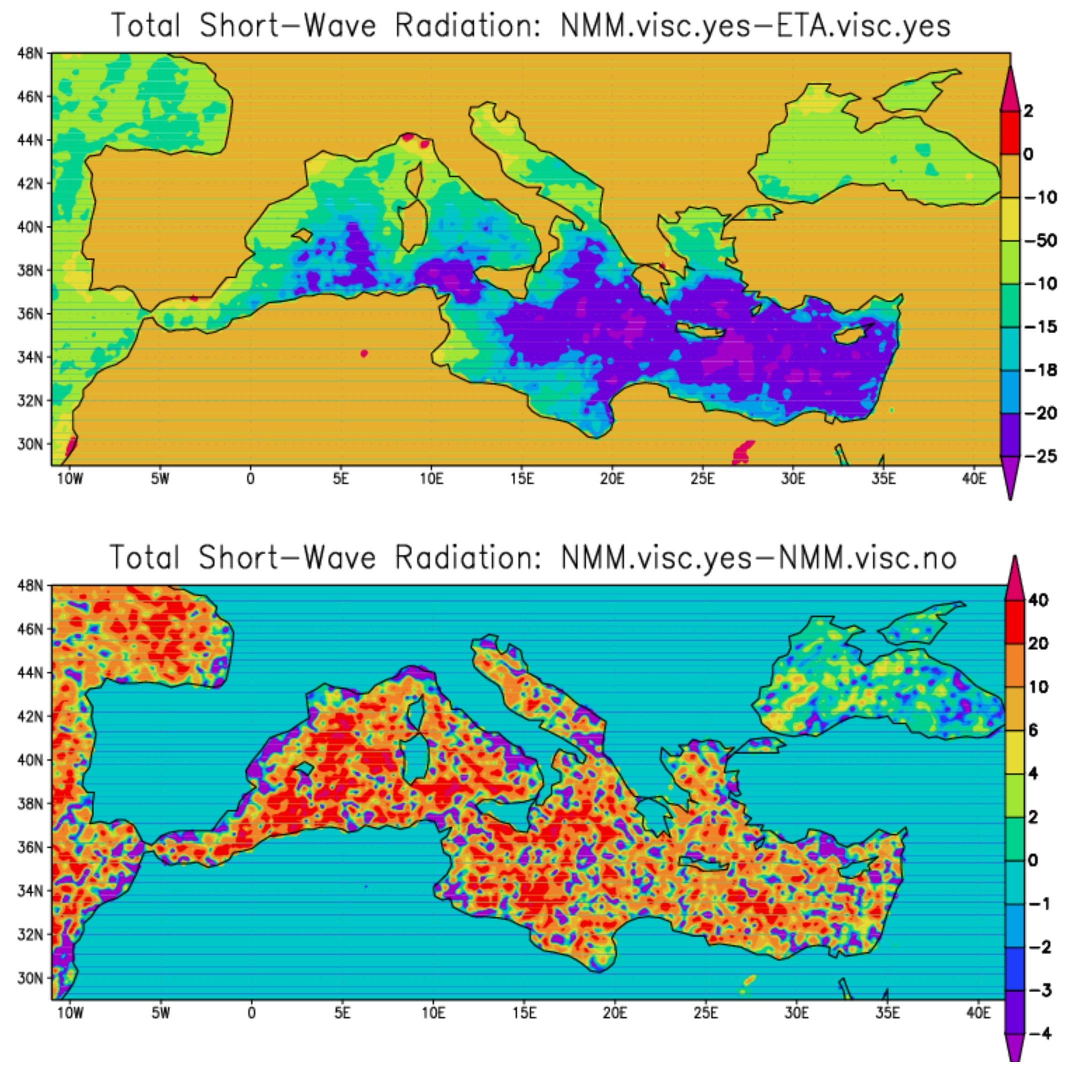

Figure 12. Simulated monthly means of total incoming short-wave radiation (Wm^{-2}) valid at 12:00 UTC in the *NMM.visc.yes-ETA.visc.yes* (upper panel) and *NMM.visc.yes- NMM.visc.no* (lower panel) experiments

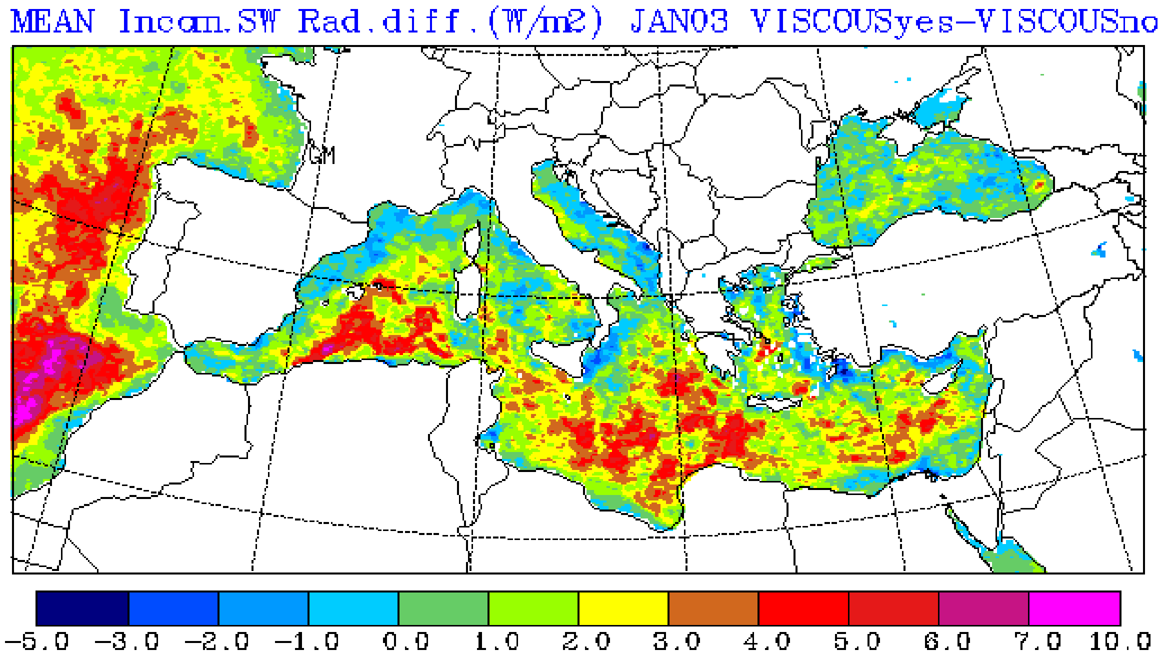

Figure 13. Monthly-mean differences of the incoming short-wave radiation between the SKIRON/Eta runs with and without the viscous sublayer in January 2003. Units: W/m^2. Positive values indicate the prediction of stronger incoming short-wave radiation when the viscous sublayer scheme is included.

Precipitation is the parameter, which contributes to the total water influx to the ocean. The experiments indicate the *ETA.visc.yes* - *NMM.visc.yes* differences (Figure 14, upper panel) to be both positive and negative with no geographical preference. However, the *NMM.visc.yes* - *NMM.visc.no* differences are negative in the largest part of the domain (Figure 14, lower panel), which could be a result of the viscous sublayer influence to the atmosphere. Similarly, SKIRON/Eta predicts smaller precipitation amounts when the viscous sublayer is included (Figure 15). In both models the largest differences appear in western Mediterranean with values up to about 0.6-0.8 mm per 12 hours (Figure 14, lower panel, and Figure 15). These results are consistent with Figure 9a that showed less upward moisture flux when the viscous effects are included.

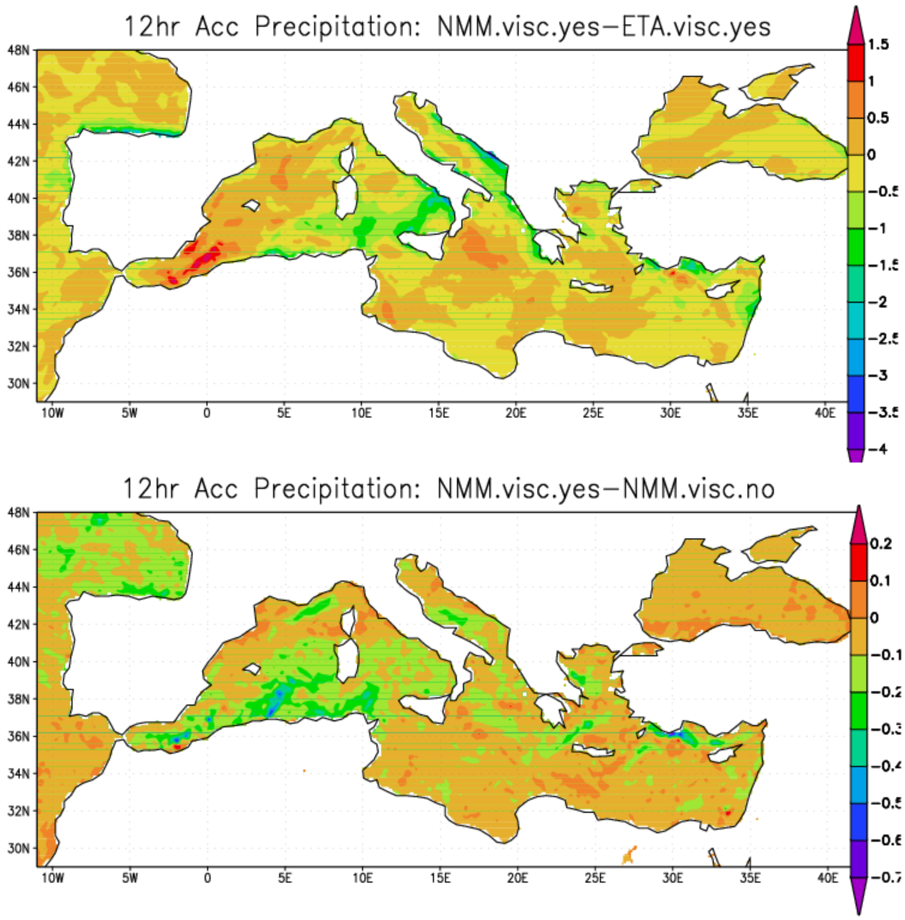

Figure 14. Simulated monthly means of 12-hr accumulated precipitation (mm) valid at 12:00 UTC in the *NMM.visc.yes-ETA.visc.yes* (upper panel) and *NMM.visc.yes- NMM.visc.no* (lower panel) experiments

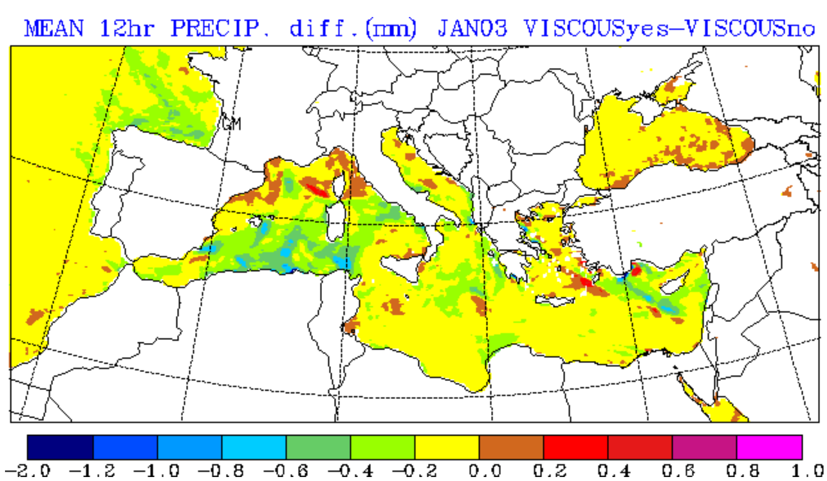

Figure 15. Monthly-mean differences of the 12-hr accumulated precipitation between the SKIRON/Eta runs with and without the viscous sublayer in January 2003. Units: mm. Positive values indicate the prediction of larger precipitation amounts when the viscous sublayer scheme is included.

Figures 16 and 17 exhibit cold temperature anomalies at 2m above sea throughout most of the Mediterranean basin in the experiments with the viscous sublayer. In both the SKIRON/Eta and the NCEP/NMM models, the largest temperature differences are simulated in the western part of the basin. This is consistent with Figure 9b that showed weaker upward sensible heat fluxes to be predicted when the viscous effects were included. The weakest sensible heat fluxes were also predicted in western Mediterranean.

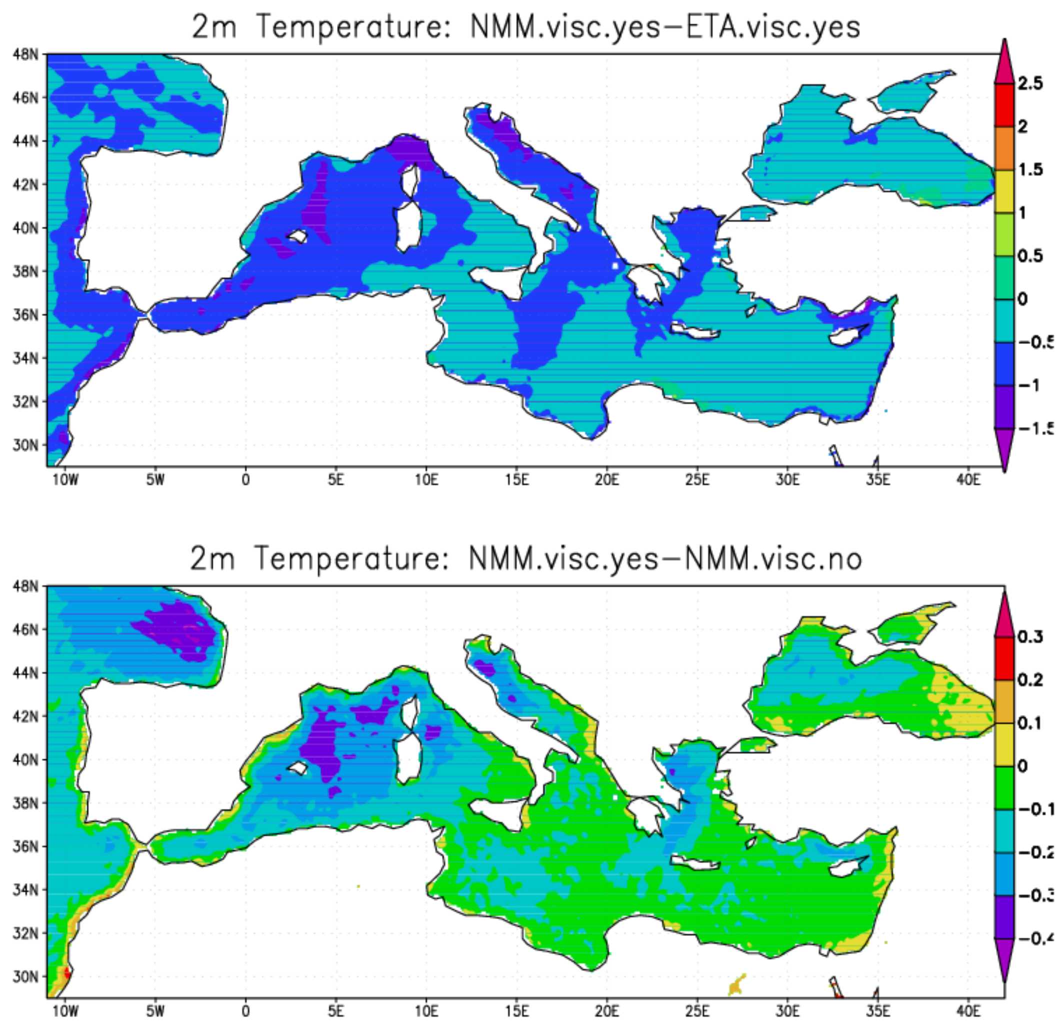

Figure 16. Simulated monthly means of 2m temperature (K) valid at 12:00 UTC in the *NMM.visc.yes-ETA.visc.yes* (upper panel) and *NMM.visc.yes- NMM.visc.no* (lower panel) experiments

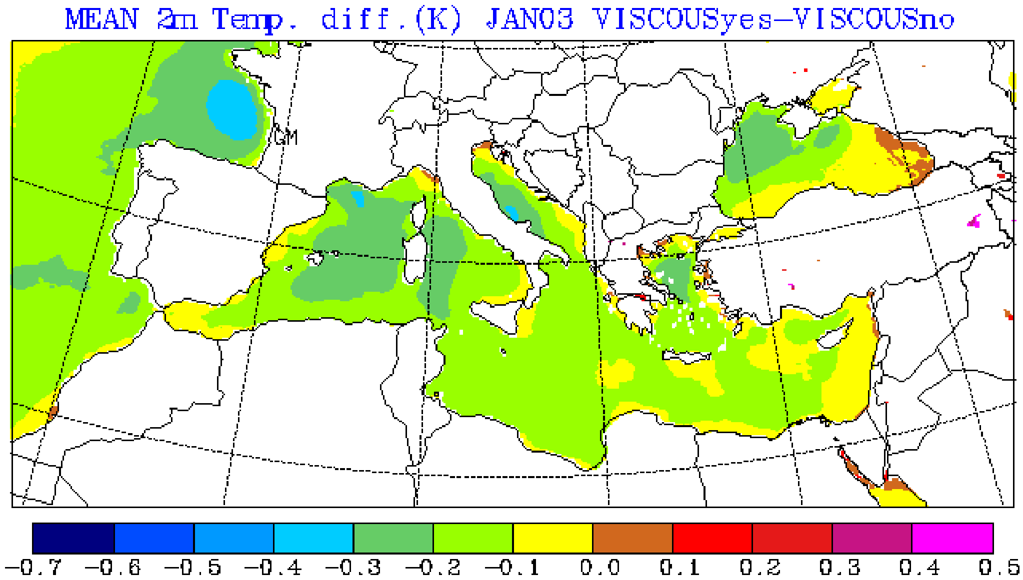

Figure 17. Monthly-mean differences of the 2m temperature between the SKIRON/Eta runs with and without the viscous sublayer in January 2003. Units: K. Positive values indicate the prediction of higher temperatures when the viscous sublayer scheme is included.

Timeseries of various model parameters, averaged over all sea model points, were calculated in order to illustrate their temporal variability in January 2003. The values were calculated with hourly and 6-hourly frequency by IASA and ICoD, respectively.

Figures 18-24 present timeseries of surface sensible heat flux, surface moisture and latent heat flux, temperature at 2m and accumulated precipitation derived by NMM.visc.no, NMM.visc.yes and ETA.visc.yes and SKIRON/Eta experiments. It can be observed that with no viscous scheme included, both SKIRON/Eta and NCEP/NMM models get consistently higher values of all three considered parameters. These results agree with the monthly-mean horizontal fields and they can be explained by the fact that without viscous sublayer only turbulent mixing exists. Turbulent mixing is stronger than molecular diffusion and thus it generates stronger fluxes. Temperature at 2m and moisture fluxes are larger while sensible heat fluxes are smaller in the NCEP/Eta than in the NCEP/NMM experiments. The momentum flux marginally differs in two NCEP/NMM cases (Figure 25).

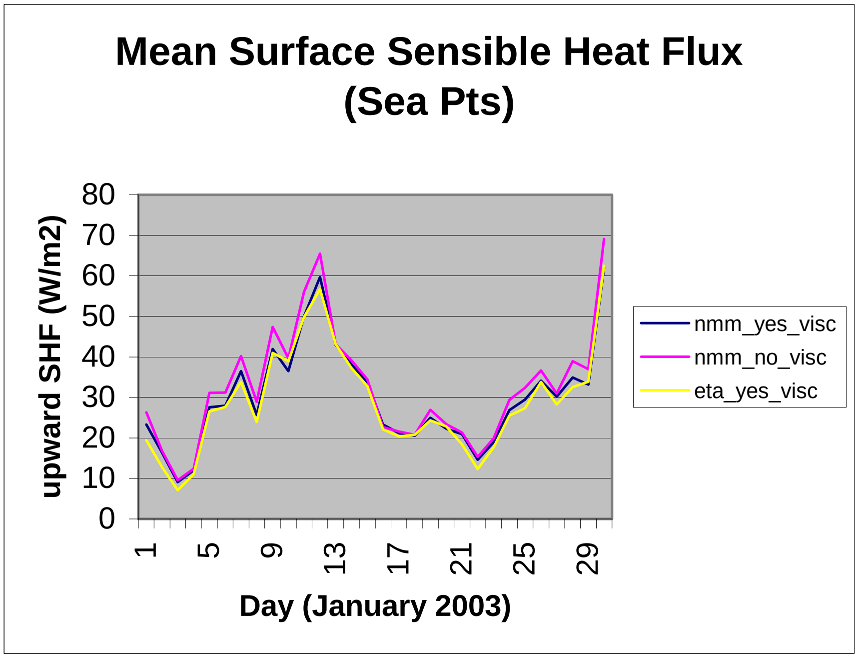

Figure 18. Simulated daily means of surface heat flux (W/m^2) averaged over all sea model points valid at 12:00 UTC in the *NMM.visc.no, NMM.visc.yes* and *ETA.visc.yes* experiments.

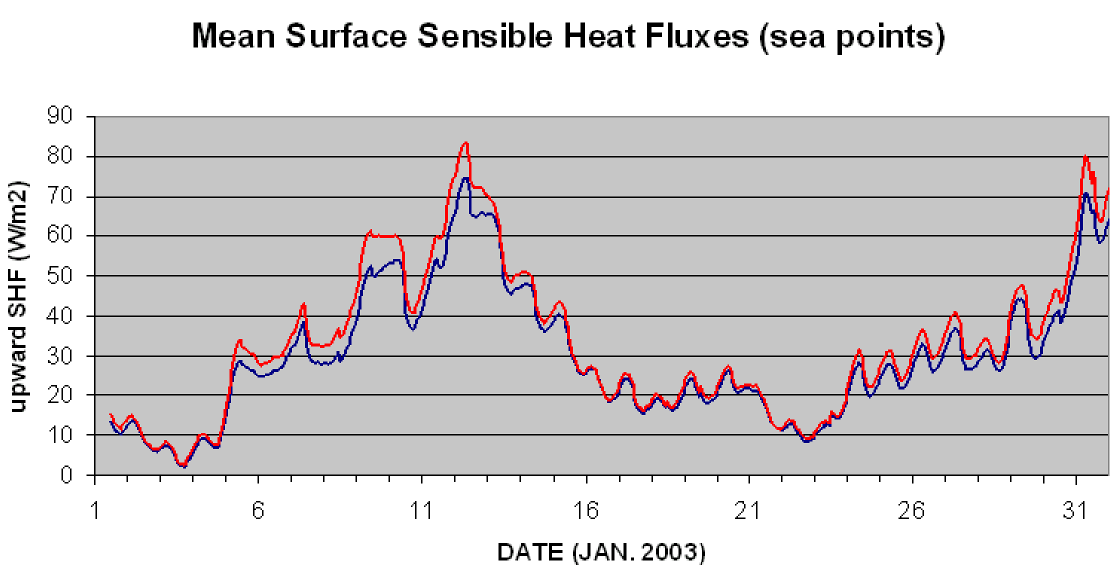

Figure 19. Hourly timeseries of the predicted surface sensible heat flux (W/m^2) averaged over all sea model points in SKIRON/Eta domain. Red line: runs without viscous sublayer, blue line: runs with viscous sublayer included.

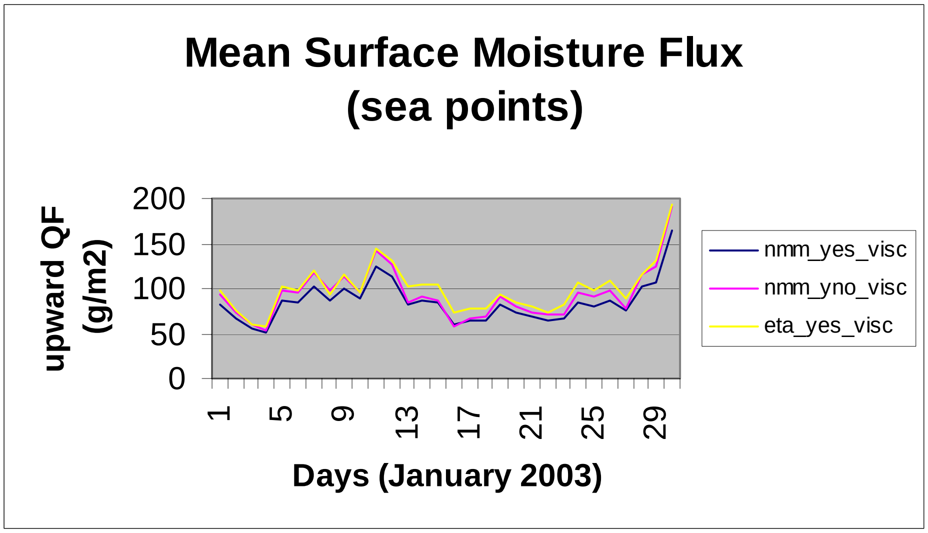

Figure 20. Simulated daily means of surface moisture flux (g/m^2) averaged over all sea model points valid at 12:00 UTC in the *NMM.visc.no, NMM.visc.yes* and *ETA.visc.yes* experiments

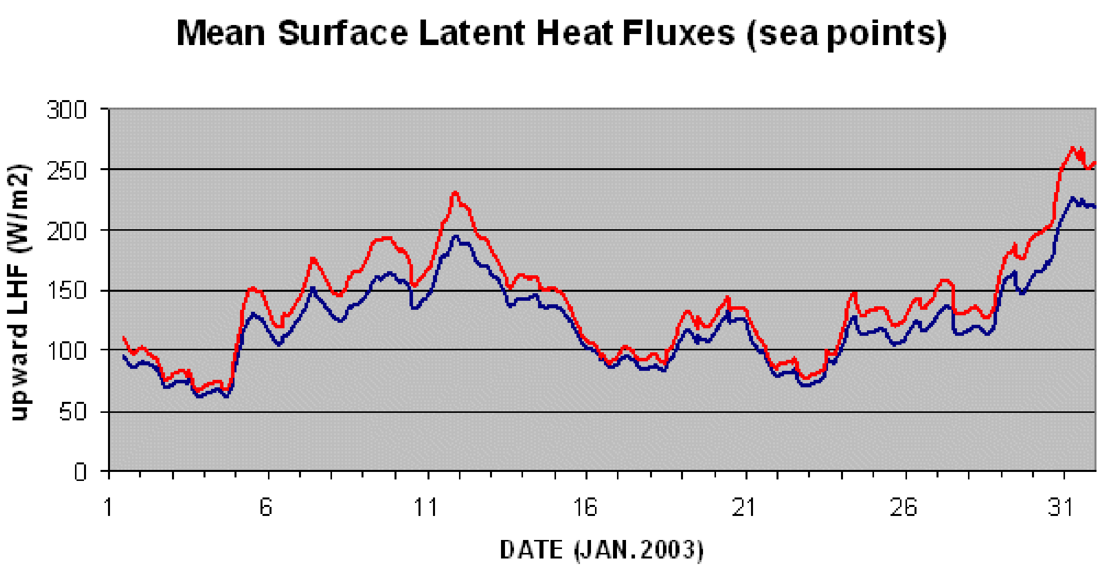

Figure 21. Hourly timeseries of the predicted surface latent heat flux (W/m^2) averaged over all sea model points in SKIRON/Eta domain. Red line: runs without viscous sublayer, blue line: runs with viscous sublayer included.

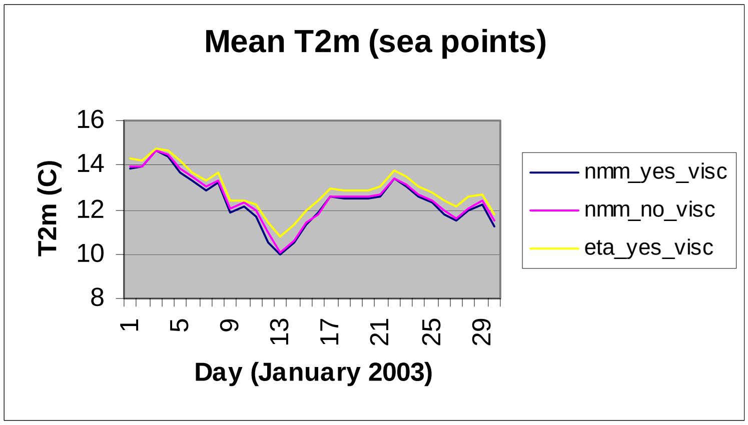

Figure 22. Simulated daily means of 2m T (C) averaged over all sea model points valid at 12:00 UTC in the *NMM.visc.no, NMM.visc.yes* and *ETA.visc.yes* experiments

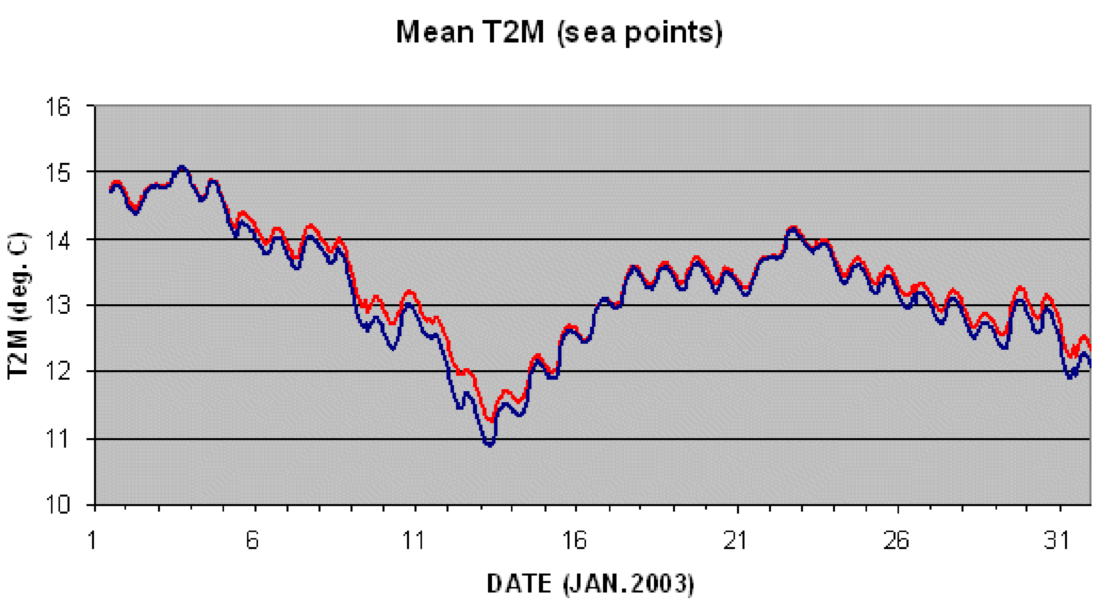

Figure 23. Hourly timeseries of the predicted 2m temperature (°C) averaged over all sea model points in SKIRON/Eta domain. Red line: runs without viscous sublayer, blue line: runs with viscous sublayer included.

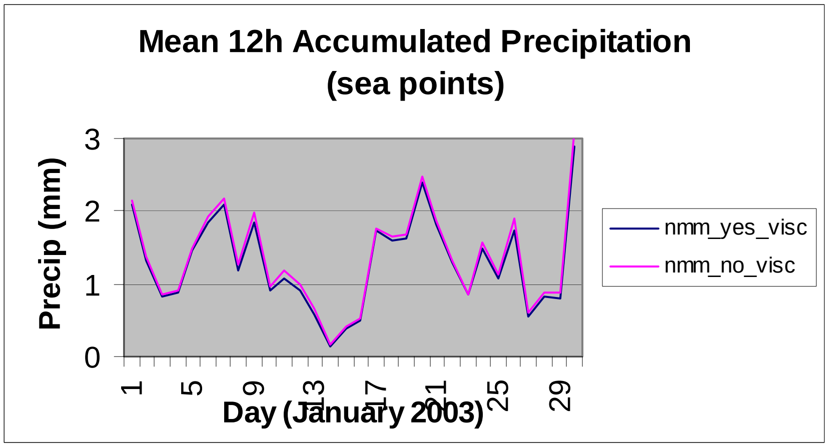

Figure 24. Simulated daily means of 12hr accumulated precipitation (mm) averaged over all sea model points valid at 12:00 UTC in the *NMM.visc.no* and *NMM.visc.yes* experiments.

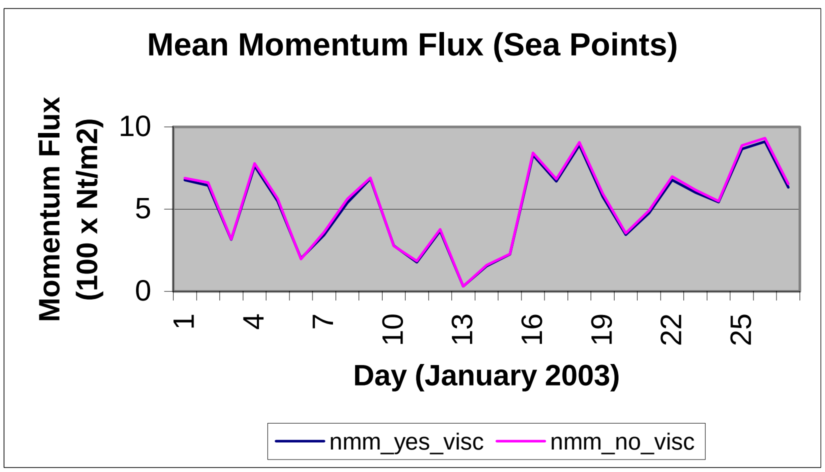

Figure 25. Simulated daily means of momentum flux (Nt/m^2) averaged over all sea model points valid at 12:00 UTC in the *NMM.visc.no* and *NMM.visc.yes* experiments

5. Conclusions

Series of experiments have been done with the SKIRON/Eta, NCEP/NMM and NCEP/Eta models in order to explore the influence of the viscous sublayer approach in calculating the fluxes at the air-sea interface. Mean values (field, daily values and timeseries over sea model points) have been calculated for that purpose. Generally, more intense turbulent mixing is obtained in tests without viscous sublayer included. However, the differences are more pronounced for the thermal fluxes/variables and less for the momentum-based flux.

This study indicates a rather important sensitivity of model results to methods applied in calculating the air-sea fluxes. Within the next Project delivery a comparison with model results with observation should indicate what of the methods is more appropriate for the atmospheric-ocean coupling purposes.

References

Adcroft, A., C. Hill and J. Marshall, 1997: Representation of topography by shaved cells in a height coordinate ocean model. *Mon. Wea. Rev.*, **125**, 2293–2315.

Ames, W. F., 1969: Numerical Methods for Partial Differential Equations. *Nelson*, London, 291 pp.

Arakawa, A. and V. R. Lamb, 1977: Computational design of the basic dynamical processes of the UCLA general circulation model. *Methods in Computational Physics, 17, Academic Press*, 173-265.

Gadd, A. J., 1974: An economical explicit integration scheme. *Meteorological Office* Techn. Note 44, 7 pp. [London Road, Bracknell, Berks. RG12 2SZ, U.K.]

Gallus W. A., Jr., 2000: The Impact of Step Orography on Flow in the Eta Model: Two Contrasting Examples. *Weather and Forecasting*:, **15**, 630–639.

Gallus W. A., Jr. and J. B. Klemp, 2000: Behavior of Flow over Step Orography. *Mon. Wea. Rev.,* **128**, 1153–1164.

Janjic, Z.I., 1977: Pressure gradient force and advection scheme used for forecasting with steep and small scale topography. *Contributions to Atmospheric Physics*, **50**, 186–199.

_________, 1979: Forward–backward scheme modified to prevent two–grid–interval noise and its application in sigma coordinate models. *Contributions to Atmospheric Physics*, **52**, 69–84.

_________, 1984: Non–linear advection schemes and energy cascade on semi–staggered grids. *Mon. Wea. Rev.*, **112**, 1234–1245.

_________, 1990: The step–mountain coordinate: physical package. *Mon.Wea.Rev.*, **118**, 1429–1443.

_________, 1994: The step–mountain eta coordinate model: further developments of the convection, viscous sublayer and turbulence closure schemes. *Mon. Wea. Rev.*, **122**, 927–945.

_________, 1996: The Surface Layer Parameterization in the Eta Model. Third Summer School in Meteorology, Krivaja, Yugoslavia. Lecture notes, pp. 53.

Janjic, Z. and A. Wiin–Nielsen, 1977: On geostrophic adjustment and numerical procedures in a rotating fluid. *J. Atmos. Sci.*, **34**, 297–310.

Janjic, Z. I., J. P. Gerrity, Jr. and S. Nickovic, 2001: An Alternative Approach to Nonhydrostatic Modeling. *Monthly Weather Review*, Vol. **129**

Janjic, Z. I., and G. DiMego, 2001: Effects of Mountain Representation and Nonhydrostatic Dynamics in a Case of Orographic Precipitation. Preprints, Symposium on Precipitation Extremes: Prediction, Impacts and Responses. 81st Annual Meeting of the American Meteorological Society, January 14-19, 2001, Albuquerque, NM, AMS, Boston, MA

Kallos, G., 1997: The Regional weather forecasting system SKIRON. Proceedings of the Symposium on Regional Weather Prediction on Parallel Computer Environments, 15-17 October 1997, Athens, Greece. pp 9.

Kallos, G., S. Nickovic, D. Jovic, O. Kakaliagou, A. Papadopoulos, N. Misirlis, L. Boukas, N. Mimikou, 1997: The ETA model operational forecasting system and its parallel implementation. Proceedings of the 1st Workshop on Large-Scale Scientific Computations, 7-11 June, Varna, Bulgaria, pp 15.

Kallos, G., A. Voudouri, I. Pytharoulis, and O. Kakaliagou, 2001: Modeling the mercury cycle in the Mediterranean: similarities and differences with conventional air pollution modeling. 25th ITM NATO/CCMS on Air Pollution Modeling and its Application, Louvain-la-Neuve, Belgium, 67-74.

Liu, W.T., K.B. Katsaros and J.A. Businger, 1979: Bulk parametrization of air-sea exchanges of heat and water vapor including the molecular constraints at the interface. *J. Atmos. Sci.,* **36**, 1722-1735.

Mangarella, P.A., A.J. Chambers, R.L. Street, and E.Y. Hsu, 1973: Laboratory studies of evaporation and energy transfer through a wavy air-water interface. *J. Phys. Oceanogr*., **3**, 93-101.

Mesinger, F., 1984: A blocking technique for representation of mountains in atmospheric models. Riv. Meteor. Aeronaut., **44**, 195-202.

Mesinger, F., Z.I. Janjic, S. Nickovic, D. Gavrilov and D.G. Deaven, 1988: The step–mountain coordinate: model description and performance for cases of Alpine lee cyclogenesis and for a case of an Appalachian redevelopment. *Mon.Wea. Rev.*, **116**, 1493–1518.

Nickovic, S., D. Mihailovic, B. Rajkovic and A. Papadopoulos, 1998: The Weather Forecasting System SKIRON, Vol. II: Description of the Model, Department of Physics, University of Athens, pp. 228

Nickovic, S., G. Kallos, A. Papadopoulos and O. Kakaliagou, 2001: A model for prediction of desert dust cycle in the atmosphere. J. Geoph. Res., **106,** 18113-18129.

Papadopoulos, A., P. Katsafados, and G. Kallos, 2002: Regional weather forecasting for marine application. GAOS, **8**, No 2-3, 219-237.

Staudenmeier, M., Jr. and J. Mittelstadt, 1998: Results of the Western Region evaluation of the Eta-10 Model. Preprints, Twelfth Conference on Numerical Weather Prediction, Phoenix, AZ, 11-16 January, 1998; AMS, Boston, MA, 131-134.

Voudouri, A., I. Pytharoulis and G. Kallos, 2005: Mercury budget estimates for the State of New York. EFM, **5**, 87-107.

Winninghoff, F. J., 1968: On the adjustment toward a geostrophic balance in a simple primitive equation model with application to the problems of initialization and objective analysis. Ph. D. Thesis, *Dept. Meteor. Univ. California*. "Dept. Meteor. Univ. California, Los Angeles, CA 90024, U.S.A.'

APPENDIX

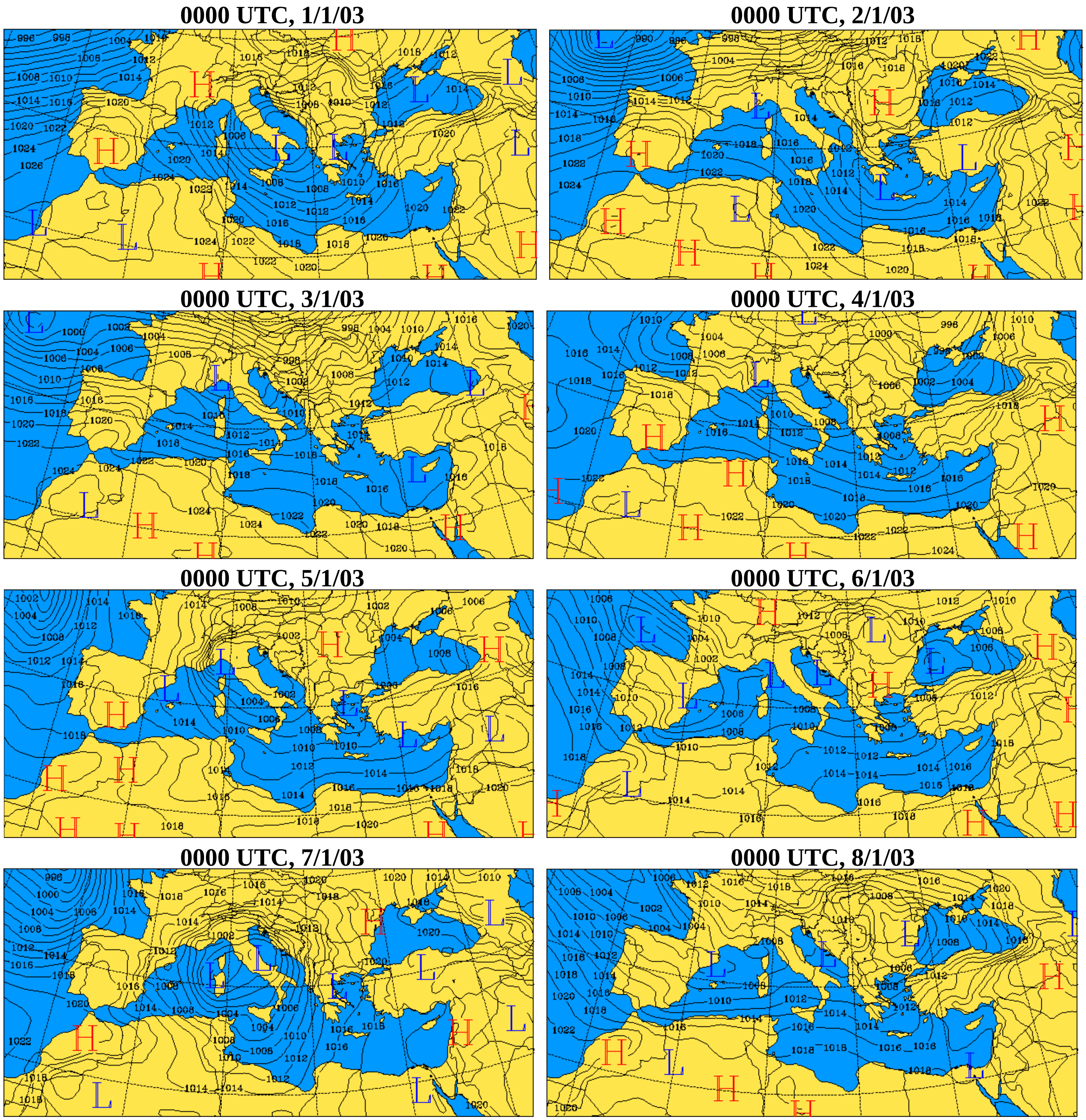

Figure A1. Mean sea-level pressure analysis charts (hPa) at 0000 UTC from 1 to 31 January 2003. Contour increment=2 hPa.

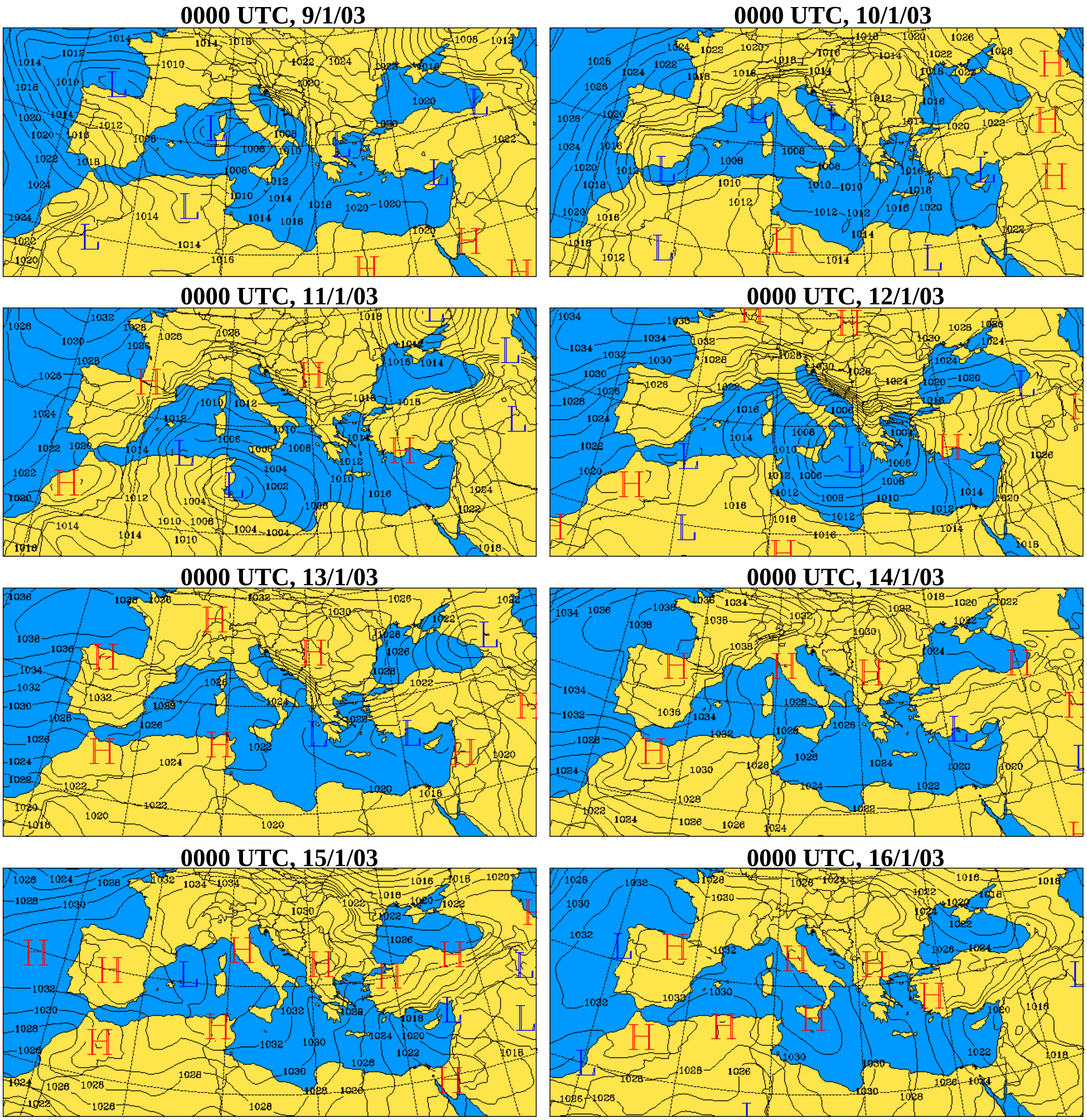

Figure A1 (continued)

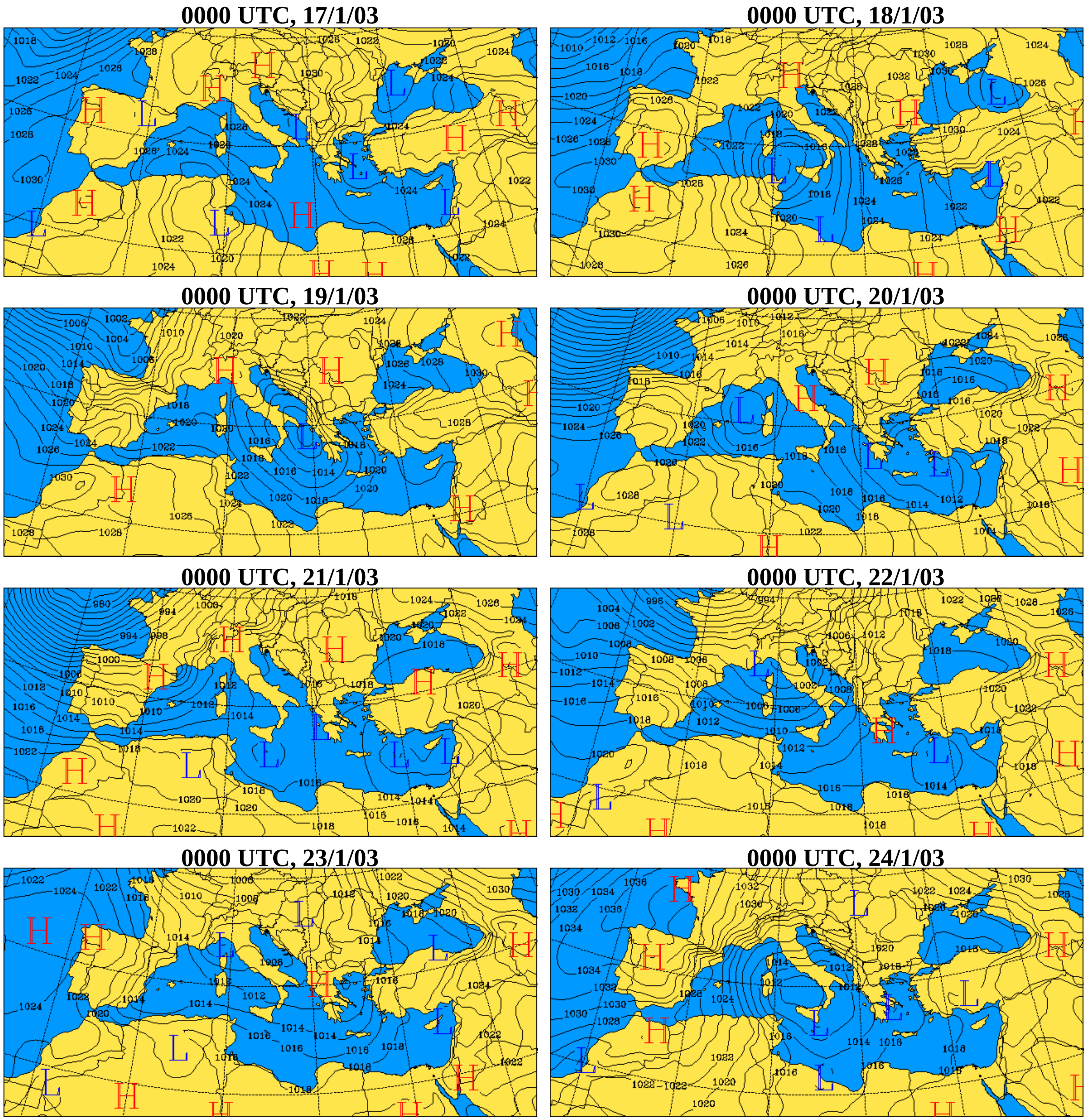

Figure A1 (continued)

0000 UTC, 25/1/03

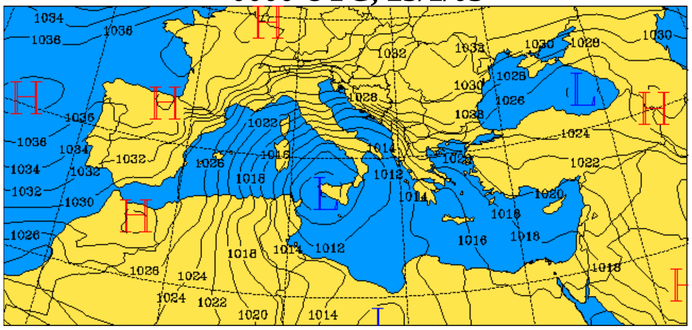

0000 UTC, 26/1/03

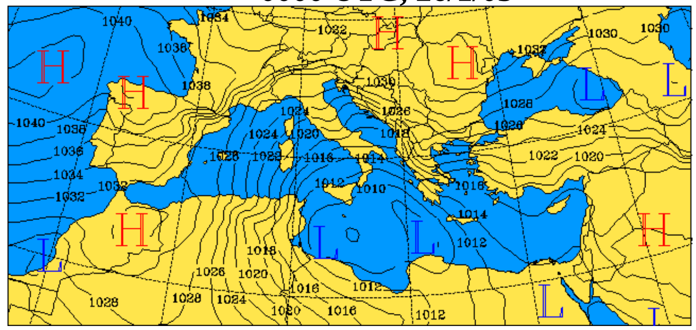

0000 UTC, 27/1/03

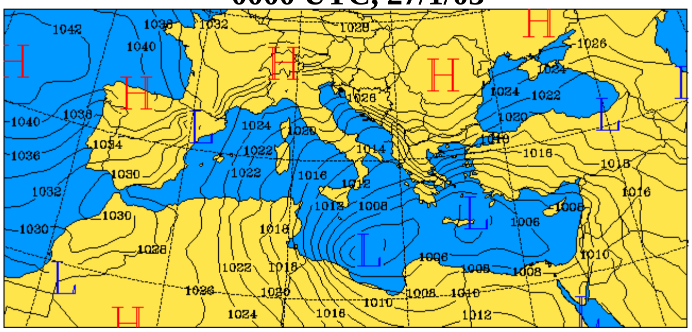

0000 UTC, 28/1/03

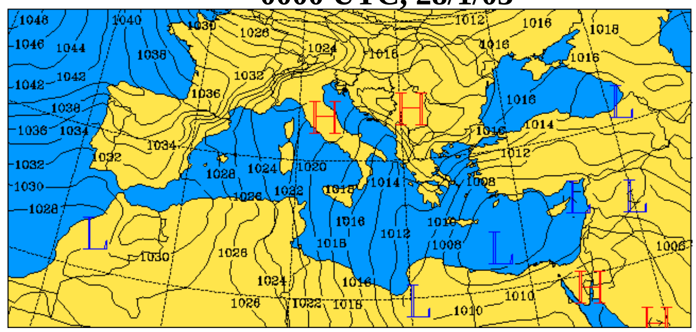

0000 UTC, 29/1/03

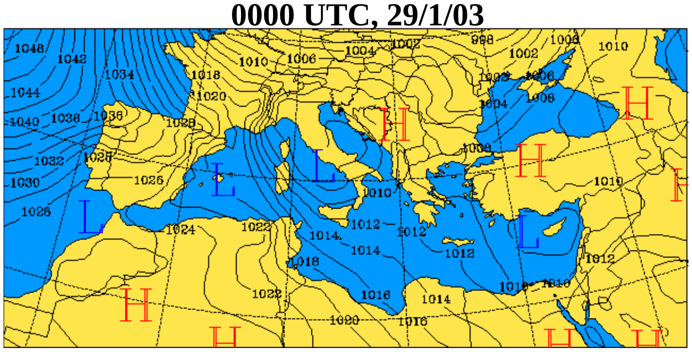

0000 UTC, 30/1/03

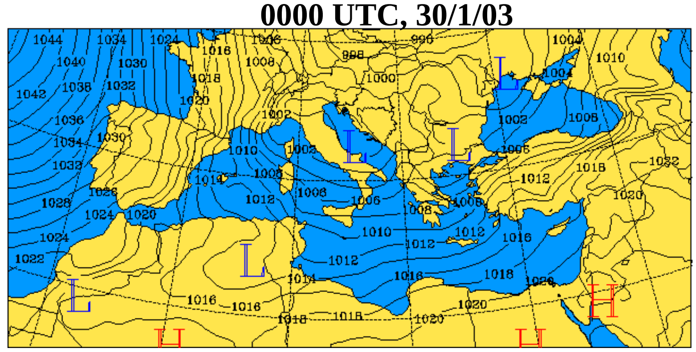

0000 UTC, 31/1/03

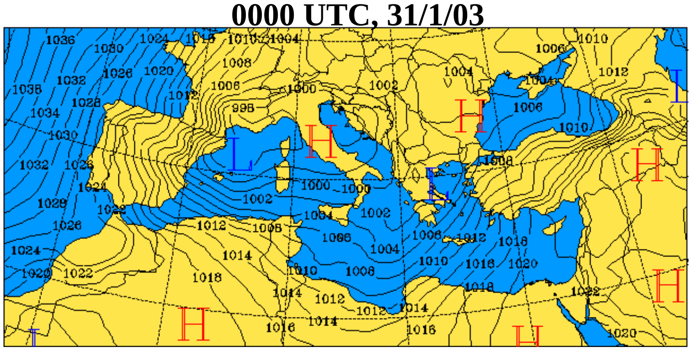

Figure A1 (continued)